



# Cu docking-activated Nb incorporation in multivariate CuO-Nb<sub>2</sub>O<sub>5</sub>/CeO<sub>2</sub> catalysts for selective reduction of NO<sub>x</sub> with NH<sub>3</sub>

Yanheng Hao<sup>a</sup>, Yan Wang<sup>b,\*</sup>, Tiantian Zhang<sup>a</sup>, Yang Liu<sup>a</sup>, Qi-Yuan Fan<sup>c,\*</sup>, Yue Jiang<sup>a</sup>,  
Yonghui Gao<sup>a</sup>, Zhihui Mao<sup>a</sup>, Xiaojun Gu<sup>a,\*</sup>, Shanghong Zeng<sup>a,\*</sup>

<sup>a</sup> Inner Mongolia Key Laboratory of Chemistry and Physics of Rare Earth Materials, School of Chemistry and Chemical Engineering, Inner Mongolia University, Hohhot 010021, China

<sup>b</sup> National Key Laboratory of Baiyunobo Rare Earth Resource Researches and Comprehensive Utilization, Baotou Research Institute of Rare Earths, Baotou 014030, China

<sup>c</sup> School of Chemistry and Chemical Engineering, Shanxi University, Taiyuan 030006, China

## ARTICLE INFO

### Keywords:

CuO  
Nb<sub>2</sub>O<sub>5</sub>  
Synergistic catalytic sites  
Oxygen vacancies  
Selective reduction

## ABSTRACT

Improving the low-temperature selective catalytic reduction of NO<sub>x</sub> with NH<sub>3</sub> (NH<sub>3</sub>-SCR) meanwhile maintaining N<sub>2</sub> selectivity are challenging in the field of catalysis. Herein, we showcase the fabrication of the synergistic catalytic sites in the CuO-Nb<sub>2</sub>O<sub>5</sub>/CeO<sub>2</sub> catalysts. Impressively, the CuO-Nb<sub>2</sub>O<sub>5</sub>/CeO<sub>2</sub> is characteristic with abundant oxygen vacancies at the interfacial regions, which facilitate the redox reaction between Ce<sup>3+</sup>, Nb<sup>5+</sup> and Cu<sup>2+</sup> with the assistance of surface oxygen, exhibiting high NH<sub>3</sub>-SCR activity, N<sub>2</sub> selectivity and wide temperature window at a gas hourly space velocity of 150,000 h<sup>-1</sup>. Contrast experiments, EXAFS analysis, in situ infrared and Raman spectroscopy, and theoretical calculations indicate that the introduction of proper copper ions in the CeO<sub>2</sub> lattice induces the structure distortion of surface CeO<sub>2</sub>, improving more niobium ions incorporation into the CeO<sub>2</sub>. The embedded Nb synergizes Cu and Ce to evoke the generation of newly adsorptive sites for NO<sub>x</sub> and NH<sub>3</sub>, thus contributing to the NH<sub>3</sub>-SCR reaction.

## 1. Introduction

Nitrogen oxides originated from the combustion of fossil fuels are major air pollutants to cause severe environmental issues, resulting in haze, acid rain, photochemical smog, and so forth [1–3]. Selective catalytic reduction of NO<sub>x</sub> with ammonia (NH<sub>3</sub>-SCR) is the most efficient technology for NO<sub>x</sub> abatement for stationary sources and automobiles. V<sub>2</sub>O<sub>5</sub>-WO<sub>3</sub>(MoO<sub>3</sub>)/TiO<sub>2</sub> and copper-exchanged SSZ-13 catalysts have been commercialized to control NO<sub>x</sub> emission from diesel vehicles [4–10]. Numerous studies have endeavored to optimize commercial NH<sub>3</sub>-SCR catalysts because the ideal catalyst is desired to possess superior low-temperature activity, high selectivity, and a wide operating temperature range.

Recently, ceria-based catalysts attract extensive attention owing to the mobility of lattice oxygen, variable valence of cations, friendly environment, high deNO<sub>x</sub> efficiency, and broad temperature window [11–13]. For instance, the amorphous Ce-Ti oxides exhibit better intrinsic SCR activity and higher N<sub>2</sub> selectivity relative to its crystalline counterpart, and the Ce-O-Ti structure was observed in FE-TEM image. A

combination of multi-characterization results confirms that the Ce-O-Ti species are the active sites during the NH<sub>3</sub>-SCR [14]. Both theoretical calculations and in situ characterization results reveal that the four-coordinated tetrahedral Ti configuration in the catalyst assures its excellent low-temperature performance [15–17]. Besides, the doped Ti can act as a SO<sub>2</sub>-trapping site, and Ce sites neighboring Ti are the main catalytically active sites for low-temperature NH<sub>3</sub>-SCR. Our group has reported that the CeO<sub>2</sub>-WO<sub>3</sub>/TiO<sub>2</sub> catalysts with surface modulation can elevate NO<sub>x</sub> conversion efficiency and broaden temperature window through improving the electron transfer on the surface [18]. Surface Ce<sub>2</sub>(SO<sub>4</sub>)<sub>3</sub> species are efficient against the alkali poisoning compared with the commercial vanadia catalysts due to adsorption and reactivity of reactants [5]. That is, precisely tuning the surface structure is paramount to enhancing SCR catalytic performance and resolving severe deactivation. Additionally, the acid centers such as Nb<sub>2</sub>O<sub>5</sub>, MoO<sub>3</sub> and WO<sub>3</sub> also play the important roles in the ceria-based catalysts, and they provide the adsorptive sites for NO<sub>x</sub> and NH<sub>3</sub>. For example, the Nb<sub>2</sub>O<sub>5</sub>/CuO/CeO<sub>2</sub> catalyst presents high deNO<sub>x</sub> activity below 200 °C and fast response in contrast with the optimal Cu zeolite catalyst [19].

\* Corresponding authors.

E-mail addresses: [wy.brيره@163.com](mailto:wy.brيره@163.com) (Y. Wang), [qyfan@sxu.edu.cn](mailto:qyfan@sxu.edu.cn) (Q.-Y. Fan), [xiaojun.gu@imu.edu.cn](mailto:xiaojun.gu@imu.edu.cn) (X. Gu), [zengshanghong@imu.edu.cn](mailto:zengshanghong@imu.edu.cn) (S. Zeng).

<https://doi.org/10.1016/j.apcatb.2023.123254>

Received 18 June 2023; Received in revised form 29 August 2023; Accepted 31 August 2023

Available online 4 September 2023

0926-3373/© 2023 Elsevier B.V. All rights reserved.

Besides, the NdV/Ti catalysts not only show low-temperature activity but also good resistance of SO<sub>2</sub> [20]. The analyses show that SO<sub>2</sub> adsorption can be prevented on the optimized catalyst, which restrains the deposition of sulfur species on the catalyst surface. Most interestingly, the synergistic interaction is revealed to have a positive effect on NO<sub>x</sub> conversion [21,22]. Altogether, these findings manifest that ceria-based catalysts have great potential for applications in NH<sub>3</sub>-SCR. Additionally, the uniform precipitates can be formed on the surface of support through microwave-assisted rapid heating [20]. Similarly, it is proposed that microwave-hydrothermal treatment can adjust the catalyst structure and improve the dispersion of active species, thus facilitating low-temperature NH<sub>3</sub>-SCR activity [23].

Hence, in this work, copper and niobium over the ceria supports were synthesized through a microwave-hydrothermal method. The intrinsic nature of CuO-Nb<sub>2</sub>O<sub>5</sub>/CeO<sub>2</sub> catalysts is unveiled through combination of characterizations and density-functional theory (DFT). The optimized sample exhibits comparable NH<sub>3</sub>-SCR activity and N<sub>2</sub> selectivity as well as wide temperature window at a gas hourly space velocity of 150,000 h<sup>-1</sup> in contrast with the reported oxide catalysts (Table S1). The most interesting finding is that the introduction of proper copper ions in the CeO<sub>2</sub> lattice induces the structure distortion of surface CeO<sub>2</sub>, improving more niobium ions incorporation into the CeO<sub>2</sub>. Furthermore, the origin of superior catalytic performance is revealed via EXAFS analysis, multiple in situ spectroscopy and DFT simulations in detail.

## 2. Experimental and computational details

### 2.1. Catalyst preparation

The CuO-Nb<sub>2</sub>O<sub>5</sub>/CeO<sub>2</sub> catalysts were synthesized via a facile microwave-hydrothermal method. In a typical procedure, an appropriate amount of Ce(NO<sub>3</sub>)<sub>3</sub>·6 H<sub>2</sub>O was dissolved in deionized water, and then NH<sub>4</sub>OH (25%) was added dropwise under magnetic stirring until the pH value of the aqueous solution was adjusted to 10.0. Next, the aqueous solution of Cu(NO<sub>3</sub>)<sub>2</sub>·3 H<sub>2</sub>O was added and stirred for 30 min, and C<sub>10</sub>H<sub>5</sub>NbO<sub>20</sub> in addition to the required volume of NH<sub>4</sub>OH was slowly dropped into the aforementioned mixture at ambient temperature. After thoroughly mixing for 30 min, the resultant mixture was transferred into a microwave system and sustained at 125 °C for 3 h. Subsequently, the obtained products were washed several times with distilled water to remove the residual impurity, then dried at 110 °C overnight, and finally calcined at 550 °C for 3 h in an air atmosphere. The composition of CuO-Nb<sub>2</sub>O<sub>5</sub>/CeO<sub>2</sub> catalysts was varied based on the change of precursor amount. They were denoted as CuO-Nb<sub>2</sub>O<sub>5</sub>/CeO<sub>2</sub>-n (n = 1, 2 and 3, see details in Table S2). For comparative study, the CuO/CeO<sub>2</sub>, Nb<sub>2</sub>O<sub>5</sub>/CeO<sub>2</sub>, Fe<sub>2</sub>O<sub>3</sub>-Nb<sub>2</sub>O<sub>5</sub>/CeO<sub>2</sub>, Co<sub>3</sub>O<sub>4</sub>-Nb<sub>2</sub>O<sub>5</sub>/CeO<sub>2</sub> and MnO<sub>2</sub>-Nb<sub>2</sub>O<sub>5</sub>/CeO<sub>2</sub> catalysts were also prepared using the same synthetic route mentioned above.

### 2.2. Steady-state catalytic activity evaluation

The NH<sub>3</sub>-SCR performances of the catalysts were tested in a fixed-bed quartz reactor with an inner diameter of 6 mm. The simulated feed gas consisted of 500 ppm of NO, 600 ppm of NH<sub>3</sub>, 200 ppm of CO, 50 ppm of C<sub>3</sub>H<sub>6</sub>, 10 vol% O<sub>2</sub>, 8 vol% CO<sub>2</sub> and 5 vol% H<sub>2</sub>O, balanced by N<sub>2</sub>, with a gas hourly space velocity (GHSV) of 150,000 h<sup>-1</sup>. The temperature was controlled in the range of 150–550 °C. An infrared gas analyzer (Antaris IGS, Thermo Scientific, USA) was used to monitor the gas concentrations of reactants and products. The experimental data were recorded after the reaction reached the steady state at every temperature point. The conversions of NO<sub>x</sub> (NO and NO<sub>2</sub>) and NH<sub>3</sub> as well as N<sub>2</sub> selectivity at various temperatures were calculated based on the Eqs. (1–3), respectively [19,24,25].

$$\text{NO}_x \text{ conversion} = \frac{[\text{NO}_x]_{\text{inlet}} - [\text{NO}_x]_{\text{outlet}}}{[\text{NO}_x]_{\text{inlet}}} \times 100\% \quad (1)$$

$$\text{NH}_3 \text{ conversion} = \frac{[\text{NH}_3]_{\text{inlet}} - [\text{NH}_3]_{\text{outlet}}}{[\text{NH}_3]_{\text{inlet}}} \times 100\% \quad (2)$$

$$\text{N}_2 \text{ selectivity} = \frac{[\text{NO}_x]_{\text{inlet}} + [\text{NH}_3]_{\text{inlet}} - [\text{NO}_x]_{\text{outlet}} - [\text{NH}_3]_{\text{outlet}} - 2[\text{N}_2\text{O}]_{\text{outlet}}}{[\text{NO}_x]_{\text{inlet}} + [\text{NH}_3]_{\text{inlet}} - [\text{NO}_x]_{\text{outlet}} - [\text{NH}_3]_{\text{outlet}}} \times 100\% \quad (3)$$

The turnover frequency (TOF) and specific reaction rate were estimated by the following Eqs. (4 and 5), respectively [18,26–28], aiming to probe the intrinsic activity of the as-synthesized catalysts. Thereinto, the physical parameters were described in the Supporting Information.

$$\text{TOF} = \frac{(\text{PV}/\text{RT})X_{\text{NO}_x}}{m_{\text{cat}}\omega/\text{M}} \quad (4)$$

$$\text{Specific reaction rate} = \frac{(\text{PV}/\text{RT})QX_{\text{NO}_x}}{wS_{\text{BET}}} \quad (5)$$

### 2.3. Characterizations, in situ DRIFTS/Raman and X-ray absorption analyses

The elemental composition in the as-prepared catalysts was determined using X-ray fluorescence (XRF) on a PANalytical Axios instrument. The crystal structure and crystallinity of various catalysts were measured by powder X-ray diffraction (XRD) with a Rigaku SmartLab SE diffractometer using a Cu Kα radiation source. Supplementary structural information of the samples was obtained under ambient conditions on a Raman spectrometer (HORIBA LabRAM Odyssey) with a 633 nm laser excitation. N<sub>2</sub>-physisorption analysis of the catalysts was conducted at liquid N<sub>2</sub> temperature using a Micromeritics ASAP2460 apparatus. The morphology, metal oxide distribution and microstructure of the samples were characterized using field-emission scanning electron microscopy (FESEM, ZEISS Sigma 500) and transmission electron microscopy (TEM, Thermo Scientific Talos F200i) equipped with an energy dispersive spectrometer (EDS) for elemental mapping. The oxidation states of the constituent elements were investigated by X-ray photoelectron spectroscopy (XPS) on a Thermo scientific ESCALAB QXi spectrometer. The reducibility and acid site distribution were measured by temperature-programmed reduction of H<sub>2</sub> (H<sub>2</sub>-TPR) and temperature-programmed desorption of NH<sub>3</sub> (NH<sub>3</sub>-TPD) on a ChemBET Pulsar chemisorption analyzer (Quantachrome, USA), respectively.

*In situ* diffuse reflectance infrared Fourier transform spectroscopy (DRIFTS) was performed on a Nicolet iS50 FTIR spectrometer, and the catalysts were placed in an in-situ quartz cell with a resolution of 4 cm<sup>-1</sup>. Initially, the catalysts were pretreated in a nitrogen atmosphere at 350 °C at a flow rate of 100 mL min<sup>-1</sup> for 0.5 h before each experiment, and then cooled down to 200 °C. Background spectra were recorded at this temperature. Next, the samples were exposed to a flow of 500 ppm of NH<sub>3</sub> with N<sub>2</sub> balance for 1 h, and then 500 ppm NO + 5% O<sub>2</sub>/N<sub>2</sub> was introduced for transient reaction studies. Conversely, 500 ppm NO + 5% O<sub>2</sub>/N<sub>2</sub> was first injected into in situ cell, and the gas flow was switched to the mixture gas of 500 ppm NH<sub>3</sub>/N<sub>2</sub>. The spectra were collected at 200 °C with time.

*In situ* Raman spectroscopy was collected in the range of 200–2000 cm<sup>-1</sup> on a HORIBA LabRAM Odyssey spectrometer equipped with a gas control system and a high-temperature cell. After catalyst pretreatment at 350 °C for 1 h in a nitrogen atmosphere (50 mL min<sup>-1</sup>), Raman spectra of the CuO-Nb<sub>2</sub>O<sub>5</sub>/CeO<sub>2</sub>-1 catalyst were obtained by heating it to the corresponding temperatures during the reaction process under flowing 500 ppm of NO, 600 ppm of NH<sub>3</sub>, 10% O<sub>2</sub> and N<sub>2</sub>.

Synchrotron X-ray absorption fine structure spectra (XAFS) were acquired with BL11B beamline at Shanghai Synchrotron Radiation

Facility (SSRF). The data were recorded at room temperature using a Si (111) crystal monochromator. The optimal  $\text{CuO-Nb}_2\text{O}_5/\text{CeO}_2$ -1 catalyst was measured in the transmission mode at Ce  $L_3$ -edge and in the fluorescence mode at Nb  $k$ -edge, respectively. The wavelet transform was implemented using a Morlet wavelet function. (See details in the [Supporting Information](#)).

#### 2.4. Computational methods and models

Spin-polarized density functional theory (DFT) calculations were implemented using the Vienna ab initio simulation package (VASP) [29,

30]. The projector augmented wave (PAW) approach with a cutoff energy of 450 eV was chosen to describe the core-valence interactions. The Perdew-Burke-Ernzerhof (PBE) functional was used to calculate the exchange-correlation energy [31–33]. We also conducted spin-polarized DFT+U calculations with a  $U_{\text{eff}}$  of 4.5 eV to accurately treat the localized Ce 4f-orbitals. The used  $U_{\text{eff}}$  value has been shown in previous studies to be able to describe the electronic structure of reduced ceria [34,35]. The convergence criterions of energy and force were set to  $10^{-5}$  eV and 0.05 eV/Å, respectively. The structures can be considered as reaching convergence when the maximum force is lower than 0.05 eV/Å.

In this work, the  $\text{CeO}_2$  (111) surface was modeled with a four-layers

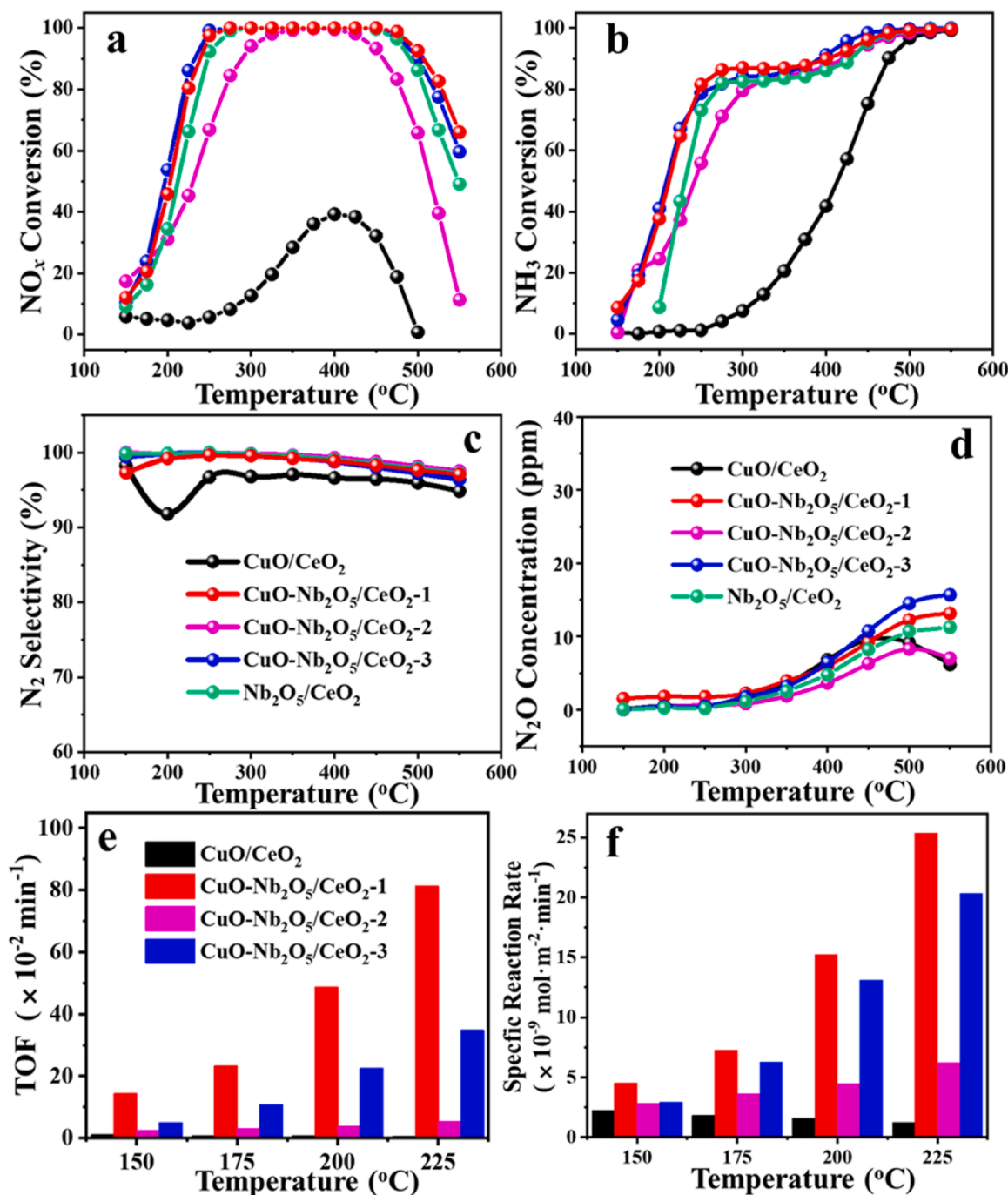


**Fig. 1.** (a)  $\text{NO}_x$  conversion, (b)  $\text{NH}_3$  conversion, (c)  $\text{N}_2$  selectivity, and (d)  $\text{N}_2\text{O}$  concentration over the  $\text{CuO/CeO}_2$ ,  $\text{Nb}_2\text{O}_5/\text{CeO}_2$  and  $\text{CuO-Nb}_2\text{O}_5/\text{CeO}_2$  catalysts as a function of the reaction temperature for the  $\text{NH}_3$ -SCR reaction. (e) TOF values normalized by the  $\text{CuO}$  sites and (f) specific reaction rate versus temperatures. The reaction feed consists of 500 ppm of  $\text{NO}$ , 600 ppm of  $\text{NH}_3$ , 200 ppm of  $\text{CO}$ , 50 ppm of  $\text{C}_3\text{H}_6$ , 10 vol%  $\text{O}_2$ , 8 vol%  $\text{CO}_2$  and 5 vol%  $\text{H}_2\text{O}$ , balanced by  $\text{N}_2$  at a GHSV of 150,000  $\text{h}^{-1}$ .

p (3 × 3) slab using a vacuum of 20 Å. A corresponding k-point mesh of (2 × 2 × 1) was used for Brillouin-zone integrations. For the model of Cu or Nb-modified CeO<sub>2</sub> (111), one surface Ce atom was replaced by one Cu or Nb atom in the top layer. Specifically, the Nb-modified Cu-CeO<sub>2</sub> (111) was modeled by substituting one Nb atom for one Ce atom around the Cu atom in the top layer. During the geometry optimization, the uppermost two layers were allowed to fully relax, while the bottom two layers were fixed. The oxygen vacancy formation energy referenced to itself ( $E_{\text{vac}}$ ) was calculated with the following Eq. (6).

$$E_{\text{vac}} = E_{\text{surf-vac}} + \frac{1}{2}E_{\text{O}_2} - E_{\text{surf}} \quad (6)$$

where the  $E_{\text{surf-vac}}$  and  $E_{\text{surf}}$  represent the total energies of a surface with and without the oxygen vacancy, respectively, and the  $E_{\text{O}_2}$  is the total energy of O<sub>2</sub> molecule in gas phase.

Additionally, the oxygen vacancy formation energy referenced to pure CeO<sub>2</sub> ( $E_{\text{vac-pure}}$ ) was calculated by the Eq. (7).

$$E_{\text{vac}} = E_{\text{surf-vac}} + \frac{1}{2}E_{\text{O}_2} - E_{\text{CeO}_2} - E_{\text{M}} \quad (7)$$

where the  $E_{\text{CeO}_2}$  represents the total energies of CeO<sub>2</sub> surface without the oxygen vacancy, and the  $E_{\text{M}}$  is the total energy of dopant (M= Cu and Nb).

### 3. Results and discussion

#### 3.1. Catalytic activity and kinetic analysis of NH<sub>3</sub>-SCR

Fig. 1a and b display the standard NH<sub>3</sub>-SCR steady-state light-off curves of the as-prepared catalysts. In stark contrast to the CuO/CeO<sub>2</sub> sample with poor SCR activity, the Nb<sub>2</sub>O<sub>5</sub>/CeO<sub>2</sub> and CuO-Nb<sub>2</sub>O<sub>5</sub>/CeO<sub>2</sub> catalysts exhibit higher NO<sub>x</sub> and NH<sub>3</sub> conversion efficiency within the examined temperature range of 150 ~ 550 °C, especially for CuO-Nb<sub>2</sub>O<sub>5</sub>/CeO<sub>2</sub>-1 and CuO-Nb<sub>2</sub>O<sub>5</sub>/CeO<sub>2</sub>-3, manifesting the mutual interaction of three oxides in enhancing NH<sub>3</sub>-SCR activity. When comparing the SCR activity of CuO-Nb<sub>2</sub>O<sub>5</sub>/CeO<sub>2</sub> with Fe<sub>2</sub>O<sub>3</sub>-Nb<sub>2</sub>O<sub>5</sub>/CeO<sub>2</sub>, Co<sub>3</sub>O<sub>4</sub>-Nb<sub>2</sub>O<sub>5</sub>/CeO<sub>2</sub> and MnO<sub>2</sub>-Nb<sub>2</sub>O<sub>5</sub>/CeO<sub>2</sub> counterparts (Fig. S1a), it is found that the presence of CuO greatly improves SCR activity, revealing the necessity of CuO in the catalyst compositions despite its low content. Wherein, it is speculated that the three species act as the synergistic catalytic sites in the NH<sub>3</sub>-SCR.

Additionally, catalytic activity of the CuO-Nb<sub>2</sub>O<sub>5</sub>/CeO<sub>2</sub> catalyst using the microwave-hydrothermal route is better than that of the CuO-Nb<sub>2</sub>O<sub>5</sub>/CeO<sub>2</sub> prepared by the conventional hydrothermal method (Fig. S1b). More specifically, a broad operation temperature window (NO<sub>x</sub> conversion above 90%) is realized over the CuO-Nb<sub>2</sub>O<sub>5</sub>/CeO<sub>2</sub>-1 and CuO-Nb<sub>2</sub>O<sub>5</sub>/CeO<sub>2</sub>-3 catalysts from 230 to 500 °C. Note that the decline of NO<sub>x</sub> conversion above 500 °C results from the NH<sub>3</sub> oxidation. Intriguingly, the CuO-Nb<sub>2</sub>O<sub>5</sub>/CeO<sub>2</sub> catalysts present a superior N<sub>2</sub> selectivity of approximately 100% in the temperature range from 150 to 450 °C (Fig. 1c). In terms of N<sub>2</sub>O formation, the CuO-Nb<sub>2</sub>O<sub>5</sub>/CeO<sub>2</sub>-1 and CuO-Nb<sub>2</sub>O<sub>5</sub>/CeO<sub>2</sub>-3 catalysts display less than 9 ppm N<sub>2</sub>O before 450 °C during the NH<sub>3</sub>-SCR reaction (Fig. 1d). Considering the high de-NO efficiency (Fig. 1a) and N<sub>2</sub> selectivity (Fig. 1c) of the CuO-Nb<sub>2</sub>O<sub>5</sub>/CeO<sub>2</sub> among the as-synthesized catalysts, the CuO-Nb<sub>2</sub>O<sub>5</sub>/CeO<sub>2</sub> catalysts were selected for the kinetic analysis of NH<sub>3</sub>-SCR.

In the cases of CuO-Nb<sub>2</sub>O<sub>5</sub>/CeO<sub>2</sub> catalysts, the relative turnover frequency (TOF) values were calculated based on the transformed mole numbers of NO<sub>x</sub> on the total CuO sites in every catalyst. As presented in Fig. 1e, the TOF values increase as the reaction temperature increases from 150 to 225 °C on the CuO-Nb<sub>2</sub>O<sub>5</sub>/CeO<sub>2</sub> catalysts. In contrast, the CuO-Nb<sub>2</sub>O<sub>5</sub>/CeO<sub>2</sub>-1 sample exhibits the highest TOF at the estimated four temperatures. Besides, the CuO-Nb<sub>2</sub>O<sub>5</sub>/CeO<sub>2</sub>-1 processes the highest TOF values at 150 and 175 °C, while the CuO-Nb<sub>2</sub>O<sub>5</sub>/CeO<sub>2</sub>-3 displays higher TOF than the CuO-Nb<sub>2</sub>O<sub>5</sub>/CeO<sub>2</sub>-1 at 200 and 225 °C

when surface niobium species are identified as the catalytically active sites (Fig. S2). These phenomena can be explained by the fact that copper and niobium species act as active sites together in the reaction, consistent with the results of NH<sub>3</sub>-SCR performances. Furthermore, the normalized specific reaction rates (Fig. 1f) follow the order of CuO-Nb<sub>2</sub>O<sub>5</sub>/CeO<sub>2</sub>-1 > CuO-Nb<sub>2</sub>O<sub>5</sub>/CeO<sub>2</sub>-3 > CuO-Nb<sub>2</sub>O<sub>5</sub>/CeO<sub>2</sub>-2 > CuO/CeO<sub>2</sub> in the calculated temperature range. Consequently, the CuO-Nb<sub>2</sub>O<sub>5</sub>/CeO<sub>2</sub>-1 catalyst is an optimal one among the as-synthesized samples. The systematic screening of the catalysts including the CuO and Nb<sub>2</sub>O<sub>5</sub> loadings, various precipitants, reaction temperatures and sequence of precipitation, as well as with/without surfactants also supports that the CuO-Nb<sub>2</sub>O<sub>5</sub>/CeO<sub>2</sub>-1 is the most effective catalyst for NH<sub>3</sub>-SCR in this work (see details in the Supporting Information from Figs. S3–S9). More specifically, the flue gas consisted of CO, N<sub>2</sub>O, NH<sub>3</sub>, C<sub>3</sub>H<sub>6</sub>, CO<sub>2</sub> and H<sub>2</sub>O when NO<sub>x</sub> conversion reaches 100% over the CuO-Nb<sub>2</sub>O<sub>5</sub>/CeO<sub>2</sub>-1 catalyst. On this basis, NO<sub>x</sub> conversion over the CuO-Nb<sub>2</sub>O<sub>5</sub>/CeO<sub>2</sub>-1 was evaluated under different experimental conditions (Fig. S10). Notably, CO and C<sub>3</sub>H<sub>6</sub> have promotional effect on the catalytic activity in this work, consistent with the previous report [36]. NO<sub>x</sub> conversion visibly decreases after sulfation at 750 °C for 1.5 h or hydrothermal aging at 750 °C for 16 h.

#### 3.2. Microscopic probing and microstructure insights

The size-uniformity, microstructure, and oxide distribution of the CuO/CeO<sub>2</sub> and CuO-Nb<sub>2</sub>O<sub>5</sub>/CeO<sub>2</sub> catalysts were characterized using SEM, TEM, HRTEM and TEM-EDS mapping. Both CuO/CeO<sub>2</sub> and CuO-Nb<sub>2</sub>O<sub>5</sub>/CeO<sub>2</sub>-1 present the morphology of irregular nanoparticles as observed in SEM and TEM images in Fig. S11 and Fig. 2, respectively. Fig. 2a and c exhibit TEM images and particle size distribution of the CuO/CeO<sub>2</sub> and CuO-Nb<sub>2</sub>O<sub>5</sub>/CeO<sub>2</sub>-1, indicating that the incorporation of niobium species induces a reduction in the size of nanoparticles. The 7.7 ± 0.2 nm nanoparticles (size statistics) are formed with respect to the CuO-Nb<sub>2</sub>O<sub>5</sub>/CeO<sub>2</sub>-1 catalyst.

High-resolution TEM observation and corresponding fast Fourier transform analysis (Fig. 2b and d) reveal the presence of well-resolved cubic-fluorite CeO<sub>2</sub> in the CuO/CeO<sub>2</sub> and CuO-Nb<sub>2</sub>O<sub>5</sub>/CeO<sub>2</sub>-1 catalysts. Lattice fringes with interplanar spacings of 0.262 or 0.267 and 0.304 or 0.306 nm are observed, consistent with the (200) and (111) crystal planes of CeO<sub>2</sub>, respectively [25,37]. Compared to the standard interplanar spacings of CeO<sub>2</sub> (0.270 nm of (200) facet, 0.312 nm of (111) plane), the reduction of interplanar spacings is possibly derived from the insertion of copper or niobium ions in the CeO<sub>2</sub> lattice. No lattice fringe of copper and niobium species are identified in HRTEM images.

(Insert: histogram of particle-size distribution (left) and fast Fourier transform (FFT, right)).

Nonetheless, the TEM-EDS elementary color-mapping of CuO-Nb<sub>2</sub>O<sub>5</sub>/CeO<sub>2</sub>-1 catalyst (Fig. 2e) further exhibits the Ce, Nb, Cu and O elements are uniformly distributed throughout the catalyst [25,38,39]. This could be explained that the copper and niobium species are highly dispersive or amorphous on the nanocrystalline-phase catalysts. As shown in Fig. 2d, the amorphous structure is observed on the surface of the Nb<sub>2</sub>O<sub>5</sub>/CeO<sub>2</sub>-1 catalyst [18].

#### 3.3. Compositional, structural identification and textural properties

The actual oxide content was determined through XRF analysis (Table S2). The measured Nb<sub>2</sub>O<sub>5</sub> content is 5.8 wt% in the CuO-Nb<sub>2</sub>O<sub>5</sub>/CeO<sub>2</sub>-2, while the Nb<sub>2</sub>O<sub>5</sub> loadings are increased to 11.7 and 17.0 wt% in the CuO-Nb<sub>2</sub>O<sub>5</sub>/CeO<sub>2</sub>-1 and CuO-Nb<sub>2</sub>O<sub>5</sub>/CeO<sub>2</sub>-3 catalysts, respectively. Meanwhile, the total CuO loading is approximately 1.0 wt% in the four samples. Coupled with the results of activity evaluation, it demonstrates that the loading amount of Nb<sub>2</sub>O<sub>5</sub> is critical to the improvement of catalytic performance, which is the reason for the low catalytic activity of the CuO-Nb<sub>2</sub>O<sub>5</sub>/CeO<sub>2</sub>-2 sample.



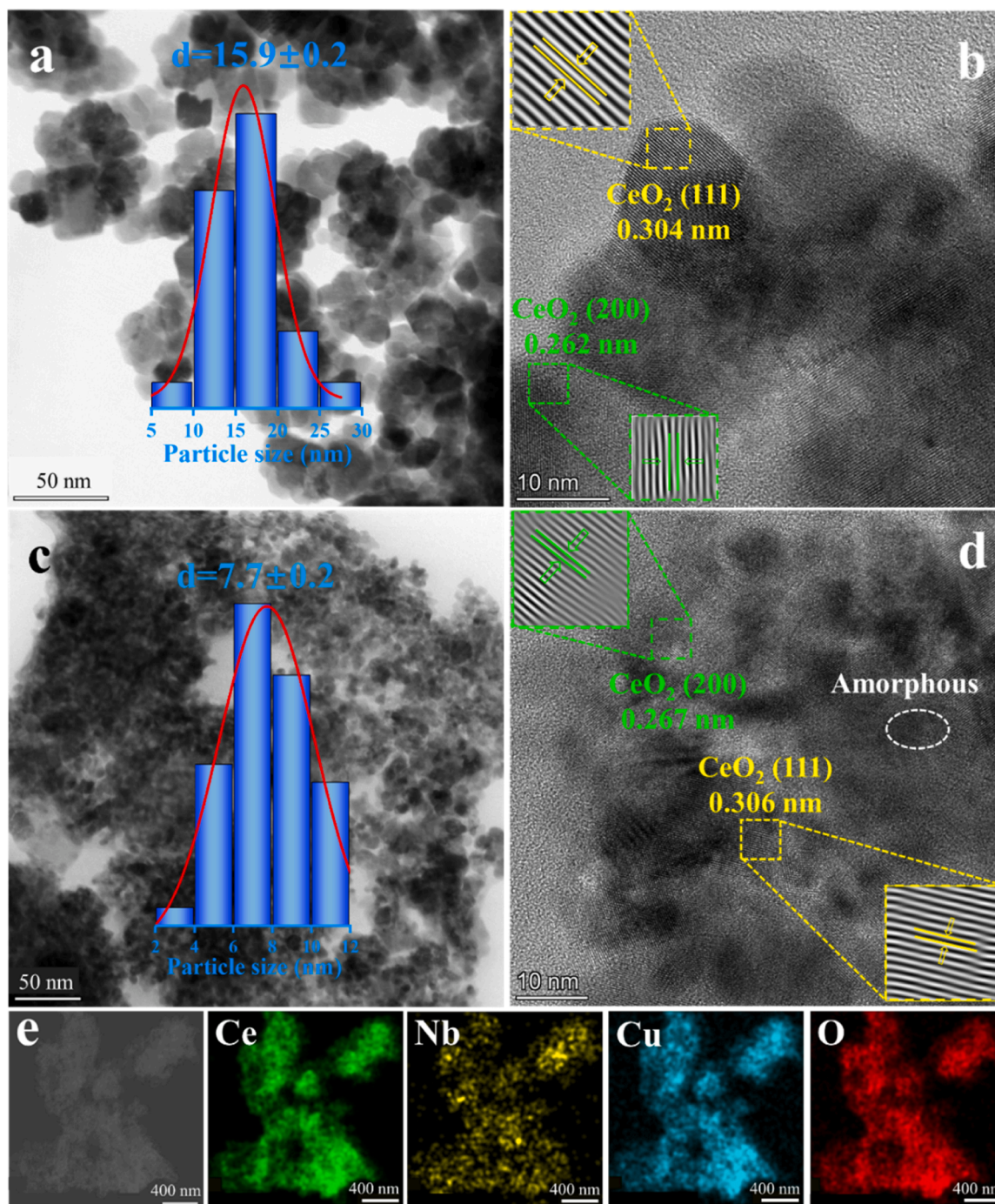


**Fig. 2.** TEM and HRTEM images of the (a, b) CuO/CeO<sub>2</sub> and (c, d) CuO-Nb<sub>2</sub>O<sub>5</sub>/CeO<sub>2</sub>-1 catalysts. (e) TEM and the corresponding elemental distribution mapping of the CuO-Nb<sub>2</sub>O<sub>5</sub>/CeO<sub>2</sub>-1 catalyst.

XRD patterns of the CuO/CeO<sub>2</sub>, Nb<sub>2</sub>O<sub>5</sub>/CeO<sub>2</sub> and CuO-Nb<sub>2</sub>O<sub>5</sub>/CeO<sub>2</sub> catalysts (Fig. 3a) exhibit the typical face-centered cubic-fluorite CeO<sub>2</sub> (space group  $Fm\bar{3}m$ , ICSD 89–8436), while no diffraction peaks assignable to Cu or Nb associated phases are observed, indicating that Cu or Nb species are present in an amorphous state or high dispersed on the catalysts [40]. Additionally, the slight offset of (111) plane characteristic peaks at 28.5° in the CuO/CeO<sub>2</sub> and CuO-Nb<sub>2</sub>O<sub>5</sub>/CeO<sub>2</sub> catalysts relative to that in the standard CeO<sub>2</sub> suggests that a portion of copper or niobium ions could incorporate into the CeO<sub>2</sub> lattice. As reported [26, 41], copper ions are easily inserted into the CeO<sub>2</sub> lattice. Moreover, a shrinkage of the lattice parameter of CeO<sub>2</sub> (Table S2) in the CuO-Nb<sub>2</sub>O<sub>5</sub>/CeO<sub>2</sub> catalysts in comparison to the CuO/CeO<sub>2</sub> (5.4113 Å)

provides the evidence that the partial Nb<sup>5+</sup> incorporates into the lattice of CeO<sub>2</sub> due to a smaller cation radius of Nb<sup>5+</sup> (0.64 Å) than that of Ce<sup>4+</sup> (0.92 Å) [42]. The incorporation of partial copper or niobium ions in the CeO<sub>2</sub> lattice provoke the valid Cu-Ce and Cu-Nb-Ce interaction [19,41]. Note that the average crystallite sizes of CeO<sub>2</sub> in the CuO-Nb<sub>2</sub>O<sub>5</sub>/CeO<sub>2</sub> catalysts (Table S2) decrease relative to that in the CuO/CeO<sub>2</sub> counterpart, corroborating that the strong interaction between Nb<sub>2</sub>O<sub>5</sub> and CeO<sub>2</sub> effectively prevents the growth of CeO<sub>2</sub> crystallites, which backs up the observation obtained from morphological characterization. This also explains the origin of the particle size disparity.

In addition to XRD studies, Raman spectra of the CuO/CeO<sub>2</sub>, Nb<sub>2</sub>O<sub>5</sub>/CeO<sub>2</sub> and CuO-Nb<sub>2</sub>O<sub>5</sub>/CeO<sub>2</sub> can provide more information on the

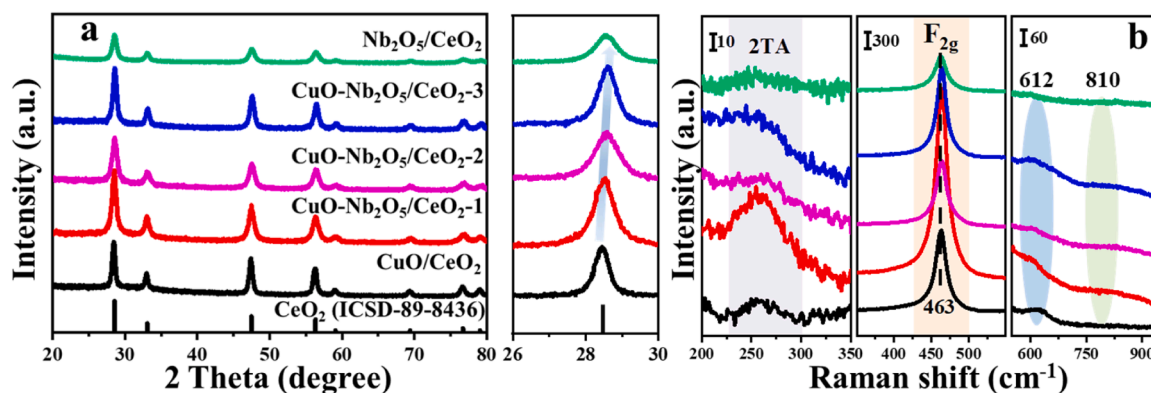


Fig. 3. (a) XRD patterns and (b) Raman spectra of the  $\text{CuO}/\text{CeO}_2$ ,  $\text{Nb}_2\text{O}_5/\text{CeO}_2$  and  $\text{CuO-Nb}_2\text{O}_5/\text{CeO}_2$  catalysts.

catalyst structure (Fig. 3b), which is more surface sensitive in contrast to XRD. For the  $\text{CuO}/\text{CeO}_2$ ,  $\text{Nb}_2\text{O}_5/\text{CeO}_2$  and  $\text{CuO-Nb}_2\text{O}_5/\text{CeO}_2$  catalysts, the band around  $258\text{ cm}^{-1}$  belongs to second order transverse acoustic (2TA) vibrational mode. The intense Raman band centered at  $463\text{ cm}^{-1}$  is assigned to the  $\text{F}_{2g}$  vibration mode of octahedral local symmetry from fluorite-type phase  $\text{CeO}_2$ , while the less pronounced band at about  $612\text{ cm}^{-1}$  corresponds to defect-induced mode originated from oxygen vacancies in the  $\text{CeO}_2$  lattice due to the incorporation of copper and niobium species [43–45]. In the case of  $\text{CuO-Nb}_2\text{O}_5/\text{CeO}_2$  catalyst, a new band at approximately  $810\text{ cm}^{-1}$  appears, attributable to highly distorted octahedrally coordinated  $\text{NbO}_6$  species, which is unsaturated Nb species with dangling bonds [46–48]. Meanwhile, no  $\text{CuO}$  and  $\text{Nb}_2\text{O}_5$  phases are detectable by Raman spectroscopy, indicative of the absence of crystalline nanoparticles, in well accordance with the finding of XRD measurements. It corroborates high dispersed state on the surface or the formation of amorphous structure. By contrast, an obvious red-shift of

Raman bands at  $612\text{ cm}^{-1}$  on the  $\text{CuO-Nb}_2\text{O}_5/\text{CeO}_2$  catalysts are observed relative to that on the  $\text{CuO}/\text{CeO}_2$ , implying a change in the electronic structure due to the interaction between  $\text{CuO}$ ,  $\text{Nb}_2\text{O}_5$  and  $\text{CeO}_2$ . Furthermore, a high intensity of 2TA vibrational mode emerges on the  $\text{CuO-Nb}_2\text{O}_5/\text{CeO}_2$ -1 sample, which is associated with the formation of lattice defects. These results reveal that the introduction of niobium species lead to the generation of distorted octahedrally coordinated  $\text{NbO}_6$  species on the  $\text{CeO}_2$  surface, which can give rise to Lewis acid sites for  $\text{NH}_3$  adsorption, simultaneously promoting the formation of Nb-O-Ce bonding and abundant oxygen vacancies. The  $\text{NH}_3$ -SCR reaction could occur along with the formation of  $\text{NbO}_6$  surface species on the  $\text{CuO-Nb}_2\text{O}_5/\text{CeO}_2$  catalysts.

$\text{N}_2$  adsorption/desorption isotherms of the  $\text{CuO}/\text{CeO}_2$ ,  $\text{Nb}_2\text{O}_5/\text{CeO}_2$  and  $\text{CuO-Nb}_2\text{O}_5/\text{CeO}_2$  catalysts present analogous shape plots, in which characteristic type-IV isotherms with a H2 hysteresis loop are observed (Fig. S12). Additionally, the BJH pore size distribution curves indicate

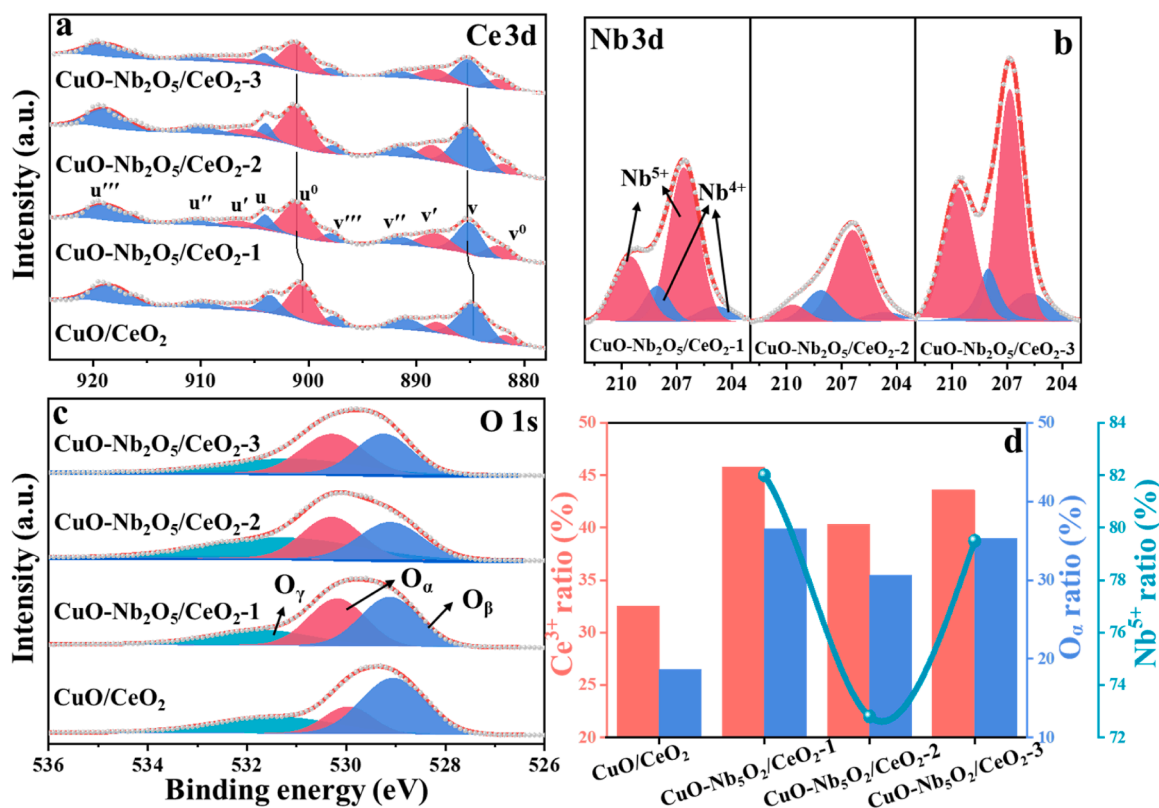


Fig. 4. High-resolution XPS spectra of Ce 3d (a), Nb 3d (b), and O 1s (c) regions over the  $\text{CuO}/\text{CeO}_2$  and  $\text{CuO-Nb}_2\text{O}_5/\text{CeO}_2$  catalysts. (d) The concentration ratios of  $\text{Ce}^{3+}$ ,  $\text{Nb}^{5+}$  and  $\text{O}_\alpha$  on the catalyst surface.



the mesoporous features. The Brunauer-Emmett-Teller (BET) surface areas, pore volume and average pore diameter are tabulated in Table S2. Interestingly, the BET surface areas increase to 36.1, 48.2 and 83.1 m<sup>2</sup> g<sup>-1</sup> after the introduction of Nb<sub>2</sub>O<sub>5</sub> in comparison to 35.1 m<sup>2</sup> g<sup>-1</sup> for the CuO/CeO<sub>2</sub>, attributable to the surface fluctuation induced by the incorporation of niobium species, which inhibits the growth of CeO<sub>2</sub> crystals and decreases the particle sizes of CeO<sub>2</sub>. Besides, the result also implies that the increase of BET surface area is related to high dispersed state and the formation of amorphous structure on the surface [49], generating a strong interaction between Nb<sub>2</sub>O<sub>5</sub> and CeO<sub>2</sub>. Consequently, it is favorable for distributing the active sites and accelerating the NH<sub>3</sub>-SCR reaction at the active sites.

### 3.4. Surface chemical states and electronic structures

The surface compositions and electronic properties of constituent elements were determined by XPS analysis. Fig. 4 and Fig. S13 present XPS spectra of the CuO/CeO<sub>2</sub>, Nb<sub>2</sub>O<sub>5</sub>/CeO<sub>2</sub> and CuO-Nb<sub>2</sub>O<sub>5</sub>/CeO<sub>2</sub> catalysts. Ce 3d XPS spectra (Fig. 4a) can be deconvoluted into ten peaks, assigned to Ce<sup>3+</sup> (v<sup>0</sup>, v<sup>1</sup>, u<sup>0</sup> and u<sup>1</sup>) and Ce<sup>4+</sup> (v<sup>2</sup>, v<sup>3</sup>, v<sup>4</sup>, u<sup>2</sup> and u<sup>3</sup>) species [50–52], respectively. The surface Ce<sup>3+</sup> concentration was estimated via the peak area ratios of Ce<sup>3+</sup>/ (Ce<sup>3+</sup> + Ce<sup>4+</sup>) in order to identify the amount of surface Ce<sup>3+</sup> species. As shown in Table S3, Fig. 4d and Fig. 13d, the surface Ce<sup>3+</sup> ratio follows the order of CuO-Nb<sub>2</sub>O<sub>5</sub>/CeO<sub>2</sub>-1 (45.8%) > CuO-Nb<sub>2</sub>O<sub>5</sub>/CeO<sub>2</sub>-3 (43.6%) > Nb<sub>2</sub>O<sub>5</sub>/CeO<sub>2</sub> (41.2%) > CuO-Nb<sub>2</sub>O<sub>5</sub>/CeO<sub>2</sub>-2 (40.3%) > CuO/CeO<sub>2</sub> (32.5%), manifesting that more Ce ions are in a low chemical valence state on the CuO-Nb<sub>2</sub>O<sub>5</sub>/CeO<sub>2</sub>-1 surface due to the interaction of Cu-Nb-Ce species. Thereinto, a higher ratio of surface Ce<sup>3+</sup> is favorable for the formation of oxygen vacancies (Table S3), resulting in the enhancement of redox ability and catalytic performance. The order of oxygen vacancies is CuO-Nb<sub>2</sub>O<sub>5</sub>/CeO<sub>2</sub>-1 (11.5) > CuO-Nb<sub>2</sub>O<sub>5</sub>/CeO<sub>2</sub>-3 (10.9) > Nb<sub>2</sub>O<sub>5</sub>/CeO<sub>2</sub> (10.3) > CuO-Nb<sub>2</sub>O<sub>5</sub>/CeO<sub>2</sub>-2 (10.0) > CuO/CeO<sub>2</sub> (8.1), which is consistent with the results of NH<sub>3</sub>-SCR activity and the specific reaction rates.

Nb 3d spectra of the CuO-Nb<sub>2</sub>O<sub>5</sub>/CeO<sub>2</sub> catalysts are exhibited in Fig. 4b. The dominant peaks centered at 206.5 and 209.5 eV with a spin-orbit splitting of 3.0 eV are ascribed to Nb 3d<sub>5/2</sub> and Nb 3d<sub>3/2</sub> signals, respectively [25,38,39]. Two Nb species were identified, corresponding to Nb<sup>5+</sup> (206.4 ~ 206.8 eV and 209.5 ~ 209.7 eV) and Nb<sup>4+</sup> species (204.6 ~ 205.7 eV and 208.0 ~ 208.1 eV) [53,54]. The presence of Nb<sup>4+</sup> is related to a redox reaction between Nb<sup>5+</sup> and Ce<sup>3+</sup> (surface oxygen vacancy), which originates from the interaction between Nb and Ce on the catalyst surface [55]. Besides, the Nb<sup>5+</sup> percentage follows the order of CuO-Nb<sub>2</sub>O<sub>5</sub>/CeO<sub>2</sub>-1 (82.0%) > CuO-Nb<sub>2</sub>O<sub>5</sub>/CeO<sub>2</sub>-3 (79.5%) > CuO-Nb<sub>2</sub>O<sub>5</sub>/CeO<sub>2</sub>-2 (72.8.3%) in Table S3 and Fig. 4d, which is in line with the trend of NH<sub>3</sub>-SCR activity and the specific reaction rates [39].

O 1 s spectra of the CuO/CeO<sub>2</sub>, Nb<sub>2</sub>O<sub>5</sub>/CeO<sub>2</sub> and CuO-Nb<sub>2</sub>O<sub>5</sub>/CeO<sub>2</sub> catalysts in Fig. 4c and Fig. S13c were fitted into three peaks, corresponding to surface chemisorbed oxygen (O<sub>α</sub>), lattice oxygen (O<sub>β</sub>) and surface adsorbed H<sub>2</sub>O or carbonate species (O<sub>γ</sub>), respectively [18,56]. As reported [18,25,38,57–59], O<sub>α</sub> is mobile and active on the catalyst surface, in favor of redox cycle of Ce<sup>3+</sup>/Ce<sup>4+</sup>. Comparatively, the CuO-Nb<sub>2</sub>O<sub>5</sub>/CeO<sub>2</sub>-1 catalyst possesses the highest surface O<sub>α</sub> ratio (Table S3 and Fig. 4d) among the as-synthesized samples, where O<sub>α</sub> accounts for a larger proportion in the O 1 s components. Note that the introduction of Nb species increases the surface O<sub>α</sub> concentration. It is proposed that Nb still has four available electrons after the incorporation of Nb species into the CeO<sub>2</sub> lattice, improving the generation of Nb-O-Ce [38]. The electron transfer from Nb to adjacent atoms on the surface through the bridged oxygen facilitates the formation of surface chemisorbed oxygen. Additionally, Cu<sup>2+</sup> and the reduced copper species coexist in the deconvoluted Cu 2p XPS spectra of the CuO-Nb<sub>2</sub>O<sub>5</sub>/CeO<sub>2</sub> (Fig. S14) and the corresponding relative percentage of Cu species is listed in Table S3. The CuO-Nb<sub>2</sub>O<sub>5</sub>/CeO<sub>2</sub>-1 catalyst exhibits the highest amount of Cu<sup>2+</sup> relative to the other counterparts. Based on the above

detailed analysis, it underscores that the CuO-Nb<sub>2</sub>O<sub>5</sub>/CeO<sub>2</sub>-1 possesses the highest Ce<sup>3+</sup>, Nb<sup>5+</sup>, Cu<sup>2+</sup> and surface O<sub>α</sub> ratio as well as rich oxygen defects among the as-prepared catalysts. The electronic coupling between Cu, Nb and Ce provokes an effective electron transfer, facilitating the generation of efficient catalytic NH<sub>3</sub>-SCR centers on the surface.

### 3.5. Acidic properties and oxide reducibility

The amount and strength of acid sites were analyzed by NH<sub>3</sub>-TPD experiments on the CuO/CeO<sub>2</sub>, Nb<sub>2</sub>O<sub>5</sub>/CeO<sub>2</sub> and CuO-Nb<sub>2</sub>O<sub>5</sub>/CeO<sub>2</sub> catalysts, and the results are shown in Fig. 5a. In the case of CuO/CeO<sub>2</sub> catalyst, a small desorption peak at 360 °C belongs to physically desorbed NH<sub>3</sub> or NH<sub>4</sub><sup>+</sup>, which is related to the weak acid sites (Brønsted acid sites) on the catalyst surface [58]. Another desorption peak at 580 °C is assigned to the NH<sub>3</sub> on the moderated acid sites (Lewis acid sites). Notably, the desorption peaks shift towards higher temperatures after the introduction of Nb<sub>2</sub>O<sub>5</sub> [19,60]. Moreover, the surface acidity was determined from the integrated peak areas of ammonia desorption (Fig. 5b). To be specific, the total acidity follows the order of CuO-Nb<sub>2</sub>O<sub>5</sub>/CeO<sub>2</sub>-1 > CuO-Nb<sub>2</sub>O<sub>5</sub>/CeO<sub>2</sub>-2 > Nb<sub>2</sub>O<sub>5</sub>/CeO<sub>2</sub> > CuO-Nb<sub>2</sub>O<sub>5</sub>/CeO<sub>2</sub>-3 > CuO/CeO<sub>2</sub>, in accordance with the trend of catalytic activity, which should be related to the activation and adsorption of NH<sub>3</sub> due to the acidity of Nb<sub>2</sub>O<sub>5</sub> during the SCR reaction.

The reduction behavior of as-prepared CuO/CeO<sub>2</sub>, Nb<sub>2</sub>O<sub>5</sub>/CeO<sub>2</sub> and CuO-Nb<sub>2</sub>O<sub>5</sub>/CeO<sub>2</sub> catalysts was experimentally investigated by H<sub>2</sub>-TPR, and the corresponding profiles are exhibited in Fig. 5c. In the case of CuO/CeO<sub>2</sub> catalyst, the reduction peaks at 239 and 295 °C are attributed to the reduction of copper oxide species [61,62], while the reduction peak at 852 °C corresponds to the reduction of bulk CeO<sub>2</sub>. For Nb<sub>2</sub>O<sub>5</sub>/CeO<sub>2</sub>, the reduction peak at 493 °C is ascribed to the reduction of surface CeO<sub>2</sub>, and the reduction peaks at 643 and 850 °C belong to the reduction of bulk CeO<sub>2</sub>. In contrast, H<sub>2</sub>-TPR profiles of the CuO-Nb<sub>2</sub>O<sub>5</sub>/CeO<sub>2</sub> catalysts are different from those of the CuO/CeO<sub>2</sub> and Nb<sub>2</sub>O<sub>5</sub>/CeO<sub>2</sub>, suggesting that Nb is well-mixed and strongly interacted with Cu and Ce. As reported [47], no reduction peak appears in H<sub>2</sub>-TPR profile of the NbO<sub>x</sub>-C from room temperature to 900 °C. Accordingly, the reduction peaks in the range of 270 ~ 600 °C are related to the reduction of copper oxide species interacting with Nb and surface CeO<sub>2</sub> [63]. Apparently, the presence of niobium oxide not only increases the reduction temperature of copper oxide species, but also greatly facilitates the reduction of surface CeO<sub>2</sub> due to the intimate contact [64]. In particular, the CuO-Nb<sub>2</sub>O<sub>5</sub>/CeO<sub>2</sub>-1 catalyst exhibits the strongest reduction peak of surface CeO<sub>2</sub> at 595 °C among the as-prepared samples, revealing the existence of abundant surface CeO<sub>2</sub> as a result of the proximity between Nb and Ce oxides. Additionally, the reduction peaks at 810 ~ 850 °C on the CuO-Nb<sub>2</sub>O<sub>5</sub>/CeO<sub>2</sub> catalysts originate from the reduction of bulk CeO<sub>2</sub>. Besides, the CuO-Nb<sub>2</sub>O<sub>5</sub>/CeO<sub>2</sub>-1 and CuO-Nb<sub>2</sub>O<sub>5</sub>/CeO<sub>2</sub>-3 catalysts have much higher total hydrogen consumption amount relative to the CuO/CeO<sub>2</sub>, Nb<sub>2</sub>O<sub>5</sub>/CeO<sub>2</sub> and CuO-Nb<sub>2</sub>O<sub>5</sub>/CeO<sub>2</sub>-2 (Fig. 5d), indicating their better redox capacity, which is beneficial to the NH<sub>3</sub>-SCR through the oxidation of NO and the activation of NH<sub>3</sub> [19, 59], in good agreement with the results of the catalytic performance.

### 3.6. Transient reactions investigated by in situ DRIFTS

To probe the adsorption and reaction process of the NH<sub>3</sub> and NO<sub>x</sub> species, in situ transient DRIFTS studies were carried out on a Nicolet iS50 FTIR spectrometer (Fig. 6a, Fig. 7 and Fig. S15). Upon exposure to 500 ppm NH<sub>3</sub>/N<sub>2</sub> at 200 °C for 60 min, the bands of pre-adsorbed NH<sub>3</sub> at 1592 and 1175 cm<sup>-1</sup> in Fig. 6a as well as 1600, 1190 and 1005 cm<sup>-1</sup> in Fig. 6c (black lines) are assigned to symmetric and asymmetric N-H bending vibrations of NH<sub>3</sub> coordinated to Lewis acid sites, respectively [25,65,66]. The bands at 1527 or 1545 cm<sup>-1</sup> belong to -NH<sub>2</sub> species [67], while the bands at 1420 cm<sup>-1</sup> are ascribed to asymmetric bending vibrations of NH<sub>4</sub><sup>+</sup> species bound to Brønsted acid sites [68,69]. Compared with the CuO/CeO<sub>2</sub> (Fig. 6a and b) [25,67], the bands

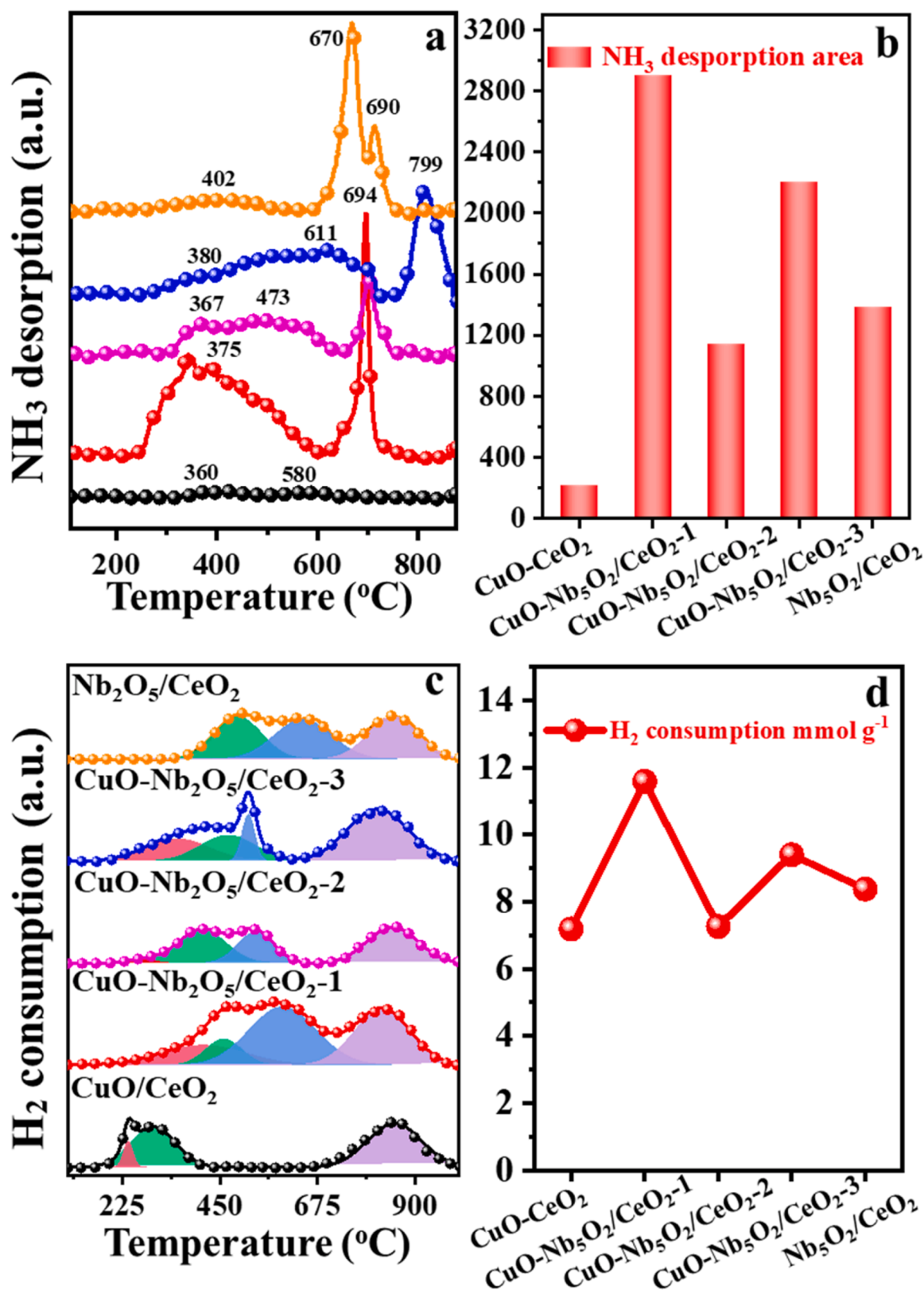
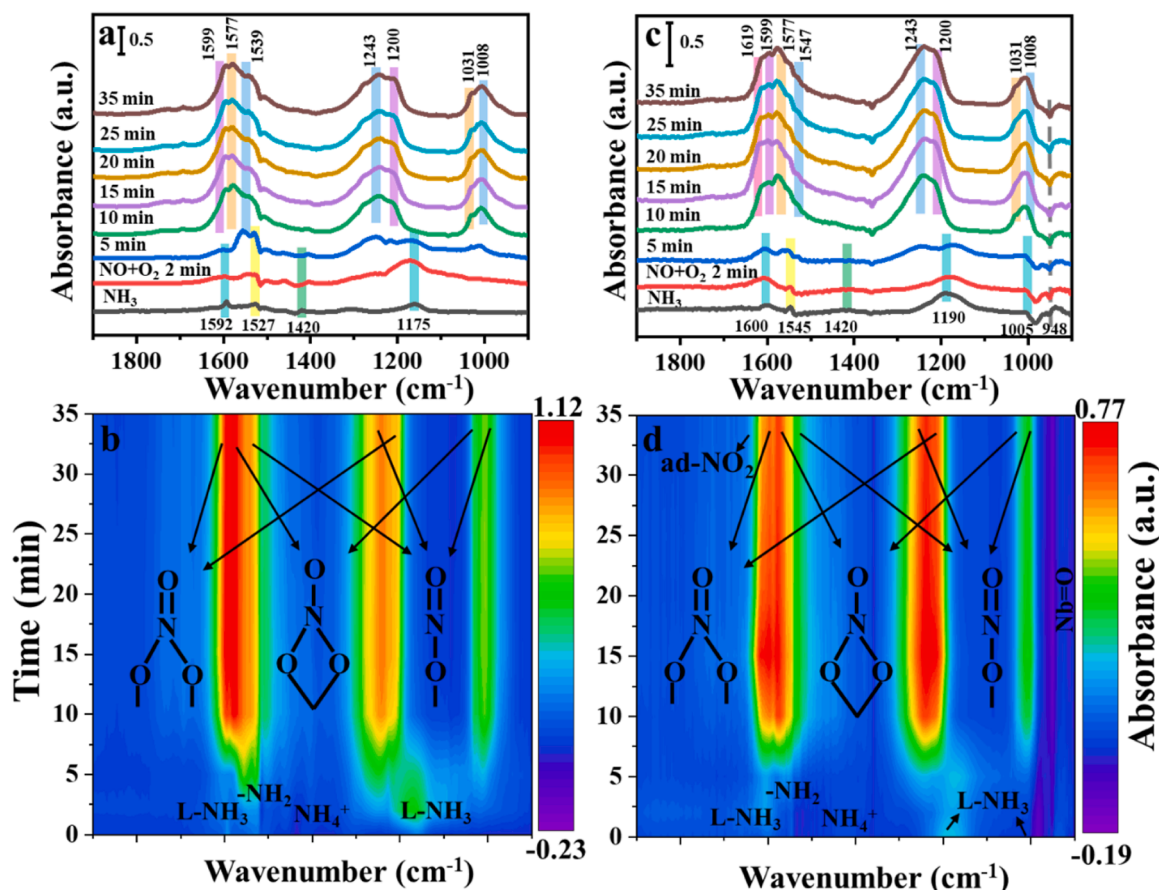


Fig. 5. (a) NH<sub>3</sub>-TPD profiles, (b) NH<sub>3</sub> desorption area, (c) H<sub>2</sub>-TPR profiles and (d) H<sub>2</sub> consumption of the CuO/CeO<sub>2</sub>, Nb<sub>2</sub>O<sub>5</sub>/CeO<sub>2</sub> and CuO-Nb<sub>2</sub>O<sub>5</sub>/CeO<sub>2</sub> catalysts.

assigned to NH<sub>3</sub> on Lewis acid sites at 1190 and 1005 cm<sup>-1</sup> increase on the CuO-Nb<sub>2</sub>O<sub>5</sub>/CeO<sub>2</sub>-1 catalyst due to the Nb<sub>2</sub>O<sub>5</sub> introduction (Fig. 6c and d) [66,67]. Besides, the negative bands at 948 cm<sup>-1</sup> correspond to adsorbed NH<sub>3</sub> on the Nb=O terminal bond [56,70]. These phenomena can be explained by the fact that the Nb<sub>2</sub>O<sub>5</sub> incorporation generates

more acid sites on the catalyst surface, in accordance with the NH<sub>3</sub>-TPD results. Subsequently, the inlet gas was switched to 500 ppm NO + 5% O<sub>2</sub>/N<sub>2</sub> in the in situ reaction cell. The intensity of pre-adsorbed NH<sub>3</sub> species gradually decreases until they disappear completely after 5 min, confirming the NH<sub>3</sub>-SCR reaction. Meanwhile, the bands assignable to





**Fig. 6.** *In situ* transient DRIFT spectra of the (a, b) CuO/CeO<sub>2</sub> and (c, d) CuO-Nb<sub>2</sub>O<sub>5</sub>/CeO<sub>2</sub>-1 catalysts. The samples were exposed to a flow of 500 ppm of NH<sub>3</sub> with N<sub>2</sub> balance for 1 h to obtain the DRIFT spectra of NH<sub>3</sub> adsorption, and then the DRIFT spectra were consecutively recorded after introducing 500 ppm NO + 5% O<sub>2</sub>/N<sub>2</sub> from 2 to 35 min.

bridging nitrates (1599 and 1200 cm<sup>-1</sup>) [71,72], bidentate nitrate (1577 and 1031 cm<sup>-1</sup>) and monodentate nitrates (1539/1547, 1243 and 1008 cm<sup>-1</sup>) appear on the CuO/CeO<sub>2</sub> and CuO-Nb<sub>2</sub>O<sub>5</sub>/CeO<sub>2</sub>-1 catalysts [56,66,73–75]. Particularly, in the case of the Nb<sub>2</sub>O<sub>5</sub>/CeO<sub>2</sub>-1, the bands at 1619 cm<sup>-1</sup> represent the absorption of NO<sub>2</sub> species [18,24], while the negative bands at 948 cm<sup>-1</sup> are associated with the NO<sub>x</sub> species adsorbed on the Nb=O bond (Fig. 6c and d) [56,70].

Furthermore, *in situ* transient DRIFTS involved in the reaction of the pre-adsorbed NO + O<sub>2</sub> with NH<sub>3</sub> were performed at 200 °C over the CuO/CeO<sub>2</sub>, Nb<sub>2</sub>O<sub>5</sub>/CeO<sub>2</sub> and CuO-Nb<sub>2</sub>O<sub>5</sub>/CeO<sub>2</sub>-1 catalysts (Fig. 7 and Fig. S15). More specifically, the bands of bridging nitrates (1599 and 1200 cm<sup>-1</sup>) [71], bidentate nitrates (1577 and 1031 cm<sup>-1</sup>) [56,73,74], and monodentate nitrates (1539/1547, 1267/1238 and 1000/1008 cm<sup>-1</sup>) are observed on the bottom black lines when the NO + 5% O<sub>2</sub>/N<sub>2</sub> was introduced into the reaction cell. Differently, the additional bands at 1278 cm<sup>-1</sup> on the CuO/CeO<sub>2</sub> correspond to bidentate nitrate (Fig. 7a and b) [56,66,75,76], while the bands at 1619 and 951 cm<sup>-1</sup> on the CuO-Nb<sub>2</sub>O<sub>5</sub>/CeO<sub>2</sub>-1 are assigned to the adsorbed NO<sub>2</sub> species and the NO<sub>x</sub> species adsorbed on the Nb=O bond (Fig. 7c and d) [18,24,56,70], respectively.

After introducing NH<sub>3</sub>/N<sub>2</sub> into the reaction cell, the bands assignable to bridging nitrates and bidentate nitrates gradually vanish with time, meanwhile the bands of monodentate nitrates at 1267/1238 cm<sup>-1</sup> also disappear after 5 min. Nonetheless, the bands attributable to monodentate nitrates at 1539/1547 and 1000/1008 cm<sup>-1</sup> remain unchanged even after 35 min. It demonstrates that the bridging nitrates and bidentate nitrates are key intermediates during NH<sub>3</sub>-SCR. Notably, the bending vibrations of NH<sub>3</sub> coordinated to Lewis acid sites are observed on these two catalysts after 5 min, while the bands attributed to

Brønsted acid sites are not found. Additionally, the negative bands at 951 cm<sup>-1</sup> corresponding to the Nb=O terminal bond also may adsorb the NH<sub>3</sub> species. Contrastively, the Nb<sub>2</sub>O<sub>5</sub> introduction in the CuO-Nb<sub>2</sub>O<sub>5</sub>/CeO<sub>2</sub>-1 catalyst boosts the formation of newly adsorptive sites for NO<sub>2</sub> and the NO<sub>x</sub> species at 1619 and 951 cm<sup>-1</sup>, respectively, facilitating the NH<sub>3</sub>-SCR reaction.

### 3.7. Structural evolution of the catalysts at elevated temperature

To monitor the structural evolution during catalysis, *in situ* Raman spectroscopy was performed on the CuO/CeO<sub>2</sub> and CuO-Nb<sub>2</sub>O<sub>5</sub>/CeO<sub>2</sub>-1 catalysts in the range of 30–550 °C. As exhibited in Fig. 8, Raman bands at 254 and 464 cm<sup>-1</sup>, attributed to the 2TA and F<sub>2g</sub> vibrational modes of fluorite structure CeO<sub>2</sub> [26,77], are observed on these two catalysts at a relatively low temperature of 150 °C. With increasing temperature to 550 °C, the bands at 254 and 464 cm<sup>-1</sup> red-shift to 244 and 454 cm<sup>-1</sup> (Δ = 10 cm<sup>-1</sup>), respectively. Based on Hooke's law, Raman shift is related to the bond length. As a result, the Ce-O is stretched due to NO<sub>x</sub> and NH<sub>3</sub> adsorption on the catalyst surface [78]. There is no evidence for the presence of CuO and Nb<sub>2</sub>O<sub>5</sub> phases, suggesting their good dispersion or in an amorphous state on the catalyst surface.

In the case of CuO/CeO<sub>2</sub> sample, no other Raman bands are observed apart from CeO<sub>2</sub> in the range of 200–2000 cm<sup>-1</sup> (Fig. S16). Nonetheless, the additional Raman bands are visible at 1050, 1308, 1371 and 1400 cm<sup>-1</sup> on the CuO-Nb<sub>2</sub>O<sub>5</sub>/CeO<sub>2</sub>-1 catalyst at 30 °C. Thereinto, the bands at 1050 cm<sup>-1</sup> are assigned to symmetric NO stretching, the bands at 1308 cm<sup>-1</sup> belong to the symmetric stretching vibration of NO<sub>3</sub>, while the bands at 1371 and 1400 cm<sup>-1</sup> are ascribed to antisymmetric N – O stretching [79–81]. Notably, these four bands shift toward a higher

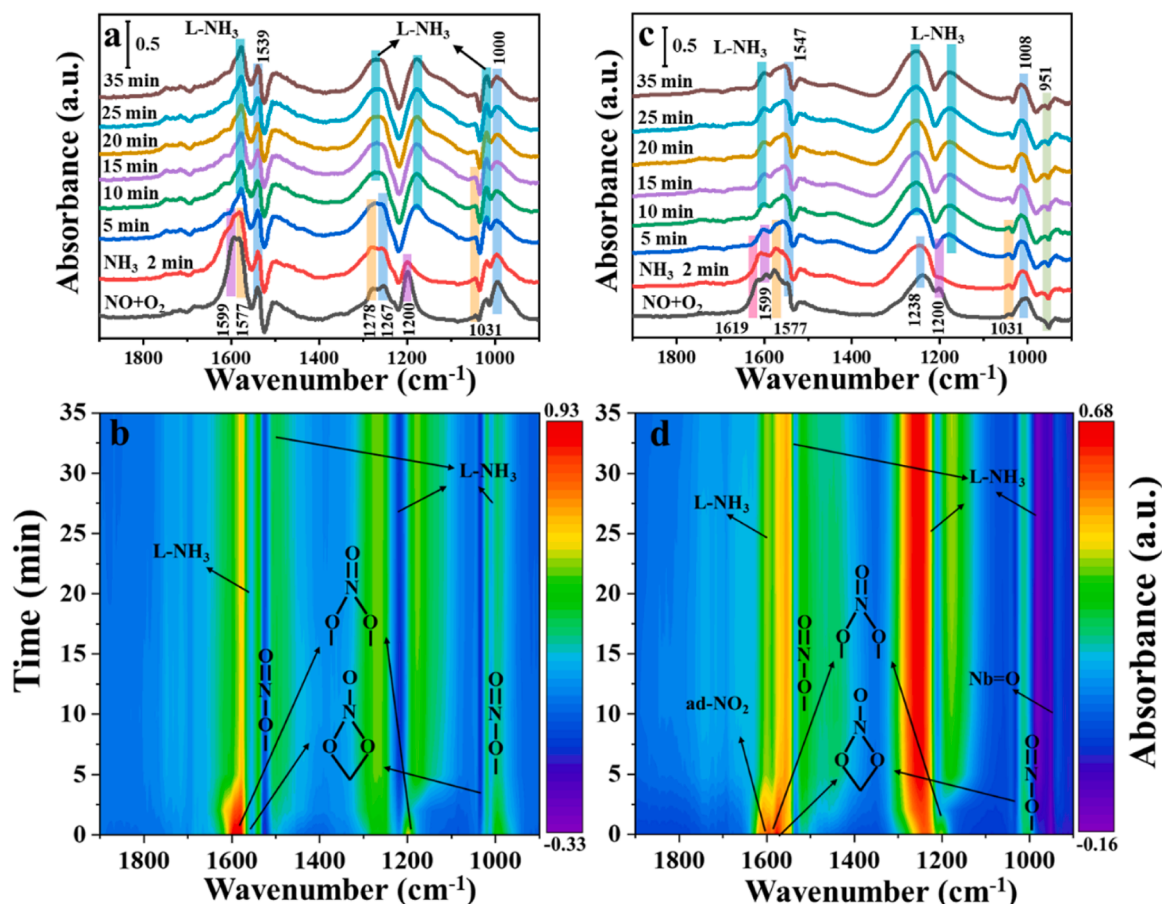


Fig. 7. *In situ* transient DRIFT spectra of the (a, b) CuO/CeO<sub>2</sub> and (c, d) CuO-Nb<sub>2</sub>O<sub>5</sub>/CeO<sub>2</sub>-1 catalysts. The samples were exposed to 500 ppm NO + 5% O<sub>2</sub>/N<sub>2</sub> at 200 °C for 1 h to obtain the DRIFT spectra of NO + O<sub>2</sub> adsorption, and then the DRIFT spectra were consecutively recorded after introducing a flow of 500 ppm of NH<sub>3</sub> with N<sub>2</sub> balance from 2 to 35 min.

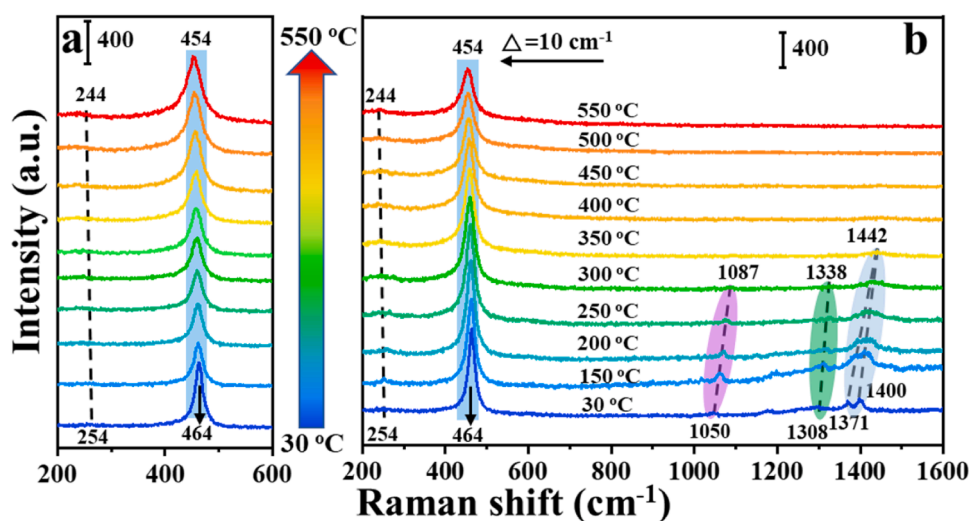


Fig. 8. *In situ* Raman spectra of the (a) CuO/CeO<sub>2</sub> and (b) CuO-Nb<sub>2</sub>O<sub>5</sub>/CeO<sub>2</sub>-1 catalysts, recorded under exposure to 500 ppm of NO, 600 ppm of NH<sub>3</sub> and 10 vol% O<sub>2</sub> in N<sub>2</sub> in the range of 30–550 °C.

wavenumber orientation with increasing temperature, reflecting the structural change of the CuO-Nb<sub>2</sub>O<sub>5</sub>/CeO<sub>2</sub>-1 catalyst during the NH<sub>3</sub>-SCR reaction. Moreover, the intensities of these bands gradually decrease as the temperature increases, and vanish above 350 °C. Collectively, these Raman spectra suggest that the Nb<sub>2</sub>O<sub>5</sub> introduction in

the CuO-Nb<sub>2</sub>O<sub>5</sub>/CeO<sub>2</sub>-1 catalyst promotes the generation of newly adsorptive sites for NO<sub>2</sub> and the NO<sub>x</sub> species relative to the CuO/CeO<sub>2</sub> sample, in good agreement with the *in situ* DRIFTS results.

### 3.8. Local bonding environment investigated through XAS

The local structure of the Ce and Nb species in the CuO-Nb<sub>2</sub>O<sub>5</sub>/CeO<sub>2</sub>-1 catalyst was characterized by X-ray absorption spectroscopy (XAS). The Ce L<sub>3</sub>-edge X-ray absorption near-edge structure (XANES) spectrum of the CuO-Nb<sub>2</sub>O<sub>5</sub>/CeO<sub>2</sub>-1 presents that the Ce species are predominantly in a Ce<sup>4+</sup> state when compared to standard CeO<sub>2</sub> and CeBr<sub>3</sub> references (Fig. 9a) [82]. Notably, the curve of the CuO-Nb<sub>2</sub>O<sub>5</sub>/CeO<sub>2</sub>-1 shows a negative edge-shift relative to that of the pristine CeO<sub>2</sub>, signifying a lower Ce valence state in contrast to CeO<sub>2</sub>, i.e., the co-existence of Ce<sup>3+</sup> and Ce<sup>4+</sup> species in the catalyst [18], as evidenced by the XPS analysis. The corresponding Ce L<sub>3</sub>-edge extended X-ray absorption fine structure (EXAFS) spectrum illustrates Ce-O and Ce-Ce bonding in the CuO-Nb<sub>2</sub>O<sub>5</sub>/CeO<sub>2</sub>-1 (Fig. 9b), similar with the standard CeO<sub>2</sub> sample [83]. Moreover, the wavelet-transform pattern from EXAFS fitting curves (Fig. S17, Fig. 9c and d) indicates the diminution of Ce-Ce bonding and the increasing contribution of Ce-O bonding in the CuO-Nb<sub>2</sub>O<sub>5</sub>/CeO<sub>2</sub>-1 sample due to the introduction of Cu and Nb species in comparison with the standard CeO<sub>2</sub>, attributable to the formation of Ce-O-Nb structure.

To explore further the origins of high activity due to the presence of Nb<sub>2</sub>O<sub>5</sub>, the Nb k-edge XANES spectra were characterized for the CuO-Nb<sub>2</sub>O<sub>5</sub>/CeO<sub>2</sub>-1 and corresponding references. From the Nb k-edge XANES spectra (Fig. 9e), the absorption edge of the CuO-Nb<sub>2</sub>O<sub>5</sub>/CeO<sub>2</sub>-1 is very close to that of Nb<sub>2</sub>O<sub>5</sub> reference [84]. The Nb-O bonding is quite similar with that in the standard Nb<sub>2</sub>O<sub>5</sub> sample in Fig. 9f (the EXAFS fitting curves are illustrated in Fig. S17), proving that Nb species are in an oxide state in the CuO-Nb<sub>2</sub>O<sub>5</sub>/CeO<sub>2</sub>-1 catalyst [85]. The absorption edge of the CuO-Nb<sub>2</sub>O<sub>5</sub>/CeO<sub>2</sub>-1 is located between Nb foil and Nb<sub>2</sub>O<sub>5</sub>, where the average valence of Nb species is between Nb<sup>0</sup> and Nb<sup>5+</sup>, in good accordance with the XPS results. Differently, the wavelet-transform pattern from EXAFS fitting curves (Fig. 9g and h) demonstrates the presence of Nb-Ce bonding in the CuO-Nb<sub>2</sub>O<sub>5</sub>/CeO<sub>2</sub>-1, inspiring the interaction between niobium and cerium [86]. Collectively, the XANES and EXAFS present clear evidence to show the existence of Nb-Ce bonding and Ce-O-Nb structure as well as the interaction derived from the insertion of copper or niobium ions in the CeO<sub>2</sub> lattice. Intriguingly, Nb in the CuO-Nb<sub>2</sub>O<sub>5</sub>/CeO<sub>2</sub>-1 catalyst is instrumental in promoting the interactions between different components.

### 3.9. Density functional theory simulations

Based on the above experimental results, four catalyst models were constructed, and the corresponding models are displayed in Fig. 10a and Fig. S18. In comparison, a notable structure distortion can be observed on Cu/CeO<sub>2</sub> (111). The Cu-O bond length is about 1.85 Å on Cu/CeO<sub>2</sub> (111) surface, which is shorter than the Ce-O bond length of 2.37 Å in the original CeO<sub>2</sub> (111). Wherein, the four oxygen atoms neighboring the Cu atom get closer to the Cu atom, and their distances from the adjacent Ce atoms increase. As a result, the Ce-O bonds are weakened accordingly, in good agreement with the previous studies [87]. Consequently, the doping of Cu atom has a positive effect on the redox ability with a lower oxygen vacancy formation energy ( $E_{\text{vac}} = -0.38$  eV) compared to pure CeO<sub>2</sub> ( $E_{\text{vac}} = 2.24$  eV). Similarly, the  $E_{\text{vac}}$  of Nb/CeO<sub>2</sub> (111) and Nb-Cu/CeO<sub>2</sub> (111) models are 0.02 and 0.38 eV, respectively, and they are also lower than that of pure CeO<sub>2</sub>, manifesting that the doping of Cu and Nb atoms are conducive to the formation of oxygen vacancies on the surface of ceria. The analysis for spin states demonstrates that the oxygens neighboring Cu atom are strongly localized (Fig. S19), confirming that the doping of Cu atom alters the electronic structure of original CeO<sub>2</sub>, as evidenced by the density of state (DOS) in Fig. 10b and c.

Aiming to shed light on the role of Cu and Nb, the oxygen vacancy formation energy that references to the pure CeO<sub>2</sub> ( $E_{\text{vac-pure}}$ ) were also calculated, as shown in Table S4. Notably, the Nb/CeO<sub>2</sub> (111) has a lower  $E_{\text{vac-pure}}$ , implying that Nb atom is more easily inserted into the

CeO<sub>2</sub> surface than Cu atom. Moreover, the energy of Nb-Cu/CeO<sub>2</sub> (111) is lower than that of Nb/CeO<sub>2</sub> (111), indicating that the incorporation of Nb species into Cu/CeO<sub>2</sub> (111) is easier than direct insertion into pure CeO<sub>2</sub>. Note that there is a more conspicuous surface distortion in terms of the Nb-Cu/CeO<sub>2</sub> (111) model. That is, one Nb-O bond and one Ce-O bond are broken, resulting in the formation of undercoordinated oxygen, which is labile and active due to the low metal-O bond breaking energy in the low coordination environment. Lastly, the adsorption energy of NH<sub>3</sub> was calculated on the models. As shown in Table S5, the Nb-Cu/CeO<sub>2</sub> (111) has a higher NH<sub>3</sub> adsorption ability compared to pure CeO<sub>2</sub>, which is favorable for the NH<sub>3</sub>-SCR activity.

Taken together, the CuO-Nb<sub>2</sub>O<sub>5</sub>/CeO<sub>2</sub> catalysts exhibit high NO<sub>x</sub> and NH<sub>3</sub> conversion efficiency and N<sub>2</sub> selectivity within the temperature range of 150 ~ 450 °C for the NH<sub>3</sub>-SCR reaction. The above experimental and theoretical investigations manifest direct evidence for the essential role of Cu and Nb species functioned as active sites in the CuO-Nb<sub>2</sub>O<sub>5</sub>/CeO<sub>2</sub>. Regarding the CuO-Nb<sub>2</sub>O<sub>5</sub>/CeO<sub>2</sub> catalyst with the synergistically active sites, the copper and niobium ions are embedded in the cubic-fluorite CeO<sub>2</sub> matrix, creating the Cu-O-Ce and Nb-O-Ce structures and abundant oxygen vacancies at the interfacial regions. Intriguingly, the incorporation of Nb species into Cu/CeO<sub>2</sub> is easier than direct insertion into pure CeO<sub>2</sub>, triggering the incorporation of more niobium ions and the generation of distorted octahedrally coordinated NbO<sub>6</sub> species on the CeO<sub>2</sub> surface. Meanwhile, the doping of Cu atom alters the electronic structure of CeO<sub>2</sub> support, and the electronic coupling between Cu, Nb and Ce provokes an effective electron transfer, facilitating the generation of catalytic NH<sub>3</sub>-SCR centers on the catalyst surface. More Ce ions are in a low chemical valence state on the CuO-Nb<sub>2</sub>O<sub>5</sub>/CeO<sub>2</sub>-1 surface due to the mutual interaction between three oxides, resulting in the formation of higher Ce<sup>3+</sup>, Nb<sup>5+</sup>, Cu<sup>2+</sup> and surface O<sub>α</sub> ratio as well as rich oxygen defects relative to the other counterparts, facilitating the redox reaction between Ce<sup>3+</sup>, Nb<sup>5+</sup> and Cu<sup>2+</sup> with the assistance of surface oxygen. Additionally, the incorporation of niobium species effectively prevents the growth of CeO<sub>2</sub> crystallites, contributes to the surface area, promotes the reduction of surface CeO<sub>2</sub> and offers Lewis acid sites for NH<sub>3</sub> adsorption.

The transient reactions from in situ DRIFTS combined with in situ Raman characterizations demonstrate that the bridging nitrates and bidentate nitrates are key intermediates during NH<sub>3</sub>-SCR, and the Nb<sub>2</sub>O<sub>5</sub> introduction in the CuO-Nb<sub>2</sub>O<sub>5</sub>/CeO<sub>2</sub>-1 catalyst promotes the generation of newly adsorptive sites for NO<sub>2</sub> and the NO<sub>x</sub> species relative to the CuO/CeO<sub>2</sub> sample, facilitating the NH<sub>3</sub>-SCR reaction. EXAFS and wavelet-transform patterns prove the existence of Nb-Ce bonding and the formation of Nb-O-Ce structure, and Nb in the CuO-Nb<sub>2</sub>O<sub>5</sub>/CeO<sub>2</sub>-1 catalyst is instrumental in promoting the interactions between different components. DFT simulations indicate that the introduction of copper ions in the CeO<sub>2</sub> matrix induces the structure distortion of surface CeO<sub>2</sub>, which is in favor of more niobium ions insertion into the CeO<sub>2</sub>, evoking the generation of rich oxygen vacancies. The defected systems are prone to contain less-coordinated highly active atomic species on the CuO-Nb<sub>2</sub>O<sub>5</sub>/CeO<sub>2</sub> surface, improving its redox capacity and facilitating the NH<sub>3</sub>-SCR through the oxidation of NO and the activation of NH<sub>3</sub>.

## 4. Conclusions

To summarize, we have demonstrated the fabrication of the synergistically active sites in the CuO-Nb<sub>2</sub>O<sub>5</sub>/CeO<sub>2</sub> catalysts through embedding the copper and niobium ions in the cubic-fluorite CeO<sub>2</sub> matrix. Through modulating the catalyst compositions and optimizing the preparation conditions, the optimal CuO-Nb<sub>2</sub>O<sub>5</sub>/CeO<sub>2</sub> exhibits comparable NH<sub>3</sub>-SCR activity and N<sub>2</sub> selectivity as well as wide temperature window at a gas hourly space velocity of 150,000 h<sup>-1</sup> in contrast with the reported oxide catalysts. Such excellent performance mainly originates from the generation of amorphous Cu-O-Ce and Nb-O-Ce structures concurrent with the formation of abundant oxygen vacancies at the interfacial regions, thus facilitating the redox reaction

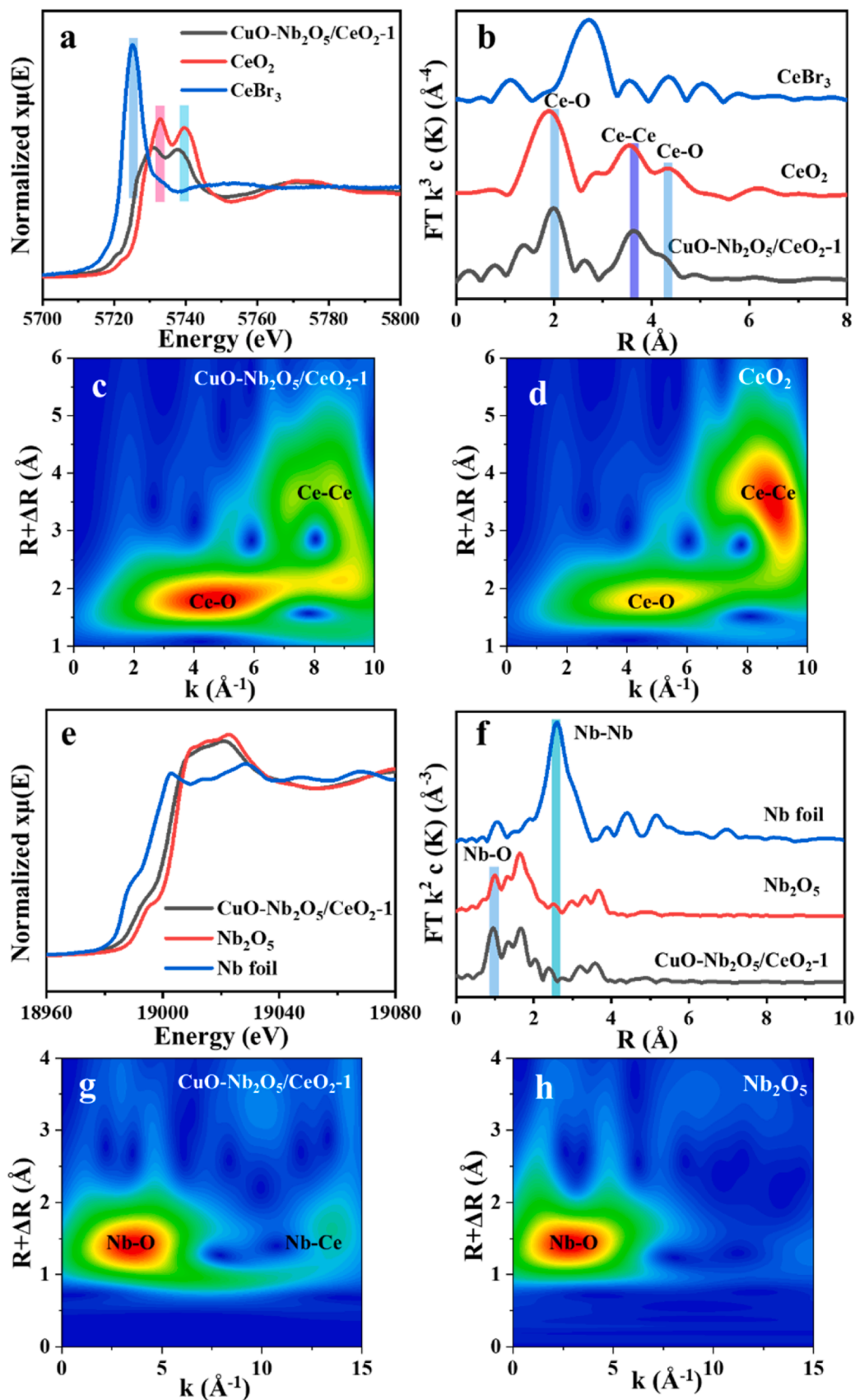


**Fig. 9.** (a) Normalized Ce L<sub>3</sub>-edge XANES spectra, (b) corresponding FT-EXAFS spectra at the R space and (c, d) wavelet transformation of Ce L<sub>3</sub>-edge EXAFS spectra of the CuO-Nb<sub>2</sub>O<sub>5</sub>/CeO<sub>2</sub>-1 and standard CeO<sub>2</sub> sample. (e) Normalized Nb k-edge XANES spectra, (f) Fourier transform EXAFS spectra at the R space and (g, h) wavelet transformation of k-edge EXAFS spectra of the CuO-Nb<sub>2</sub>O<sub>5</sub>/CeO<sub>2</sub>-1 and standard Nb<sub>2</sub>O<sub>5</sub> sample.



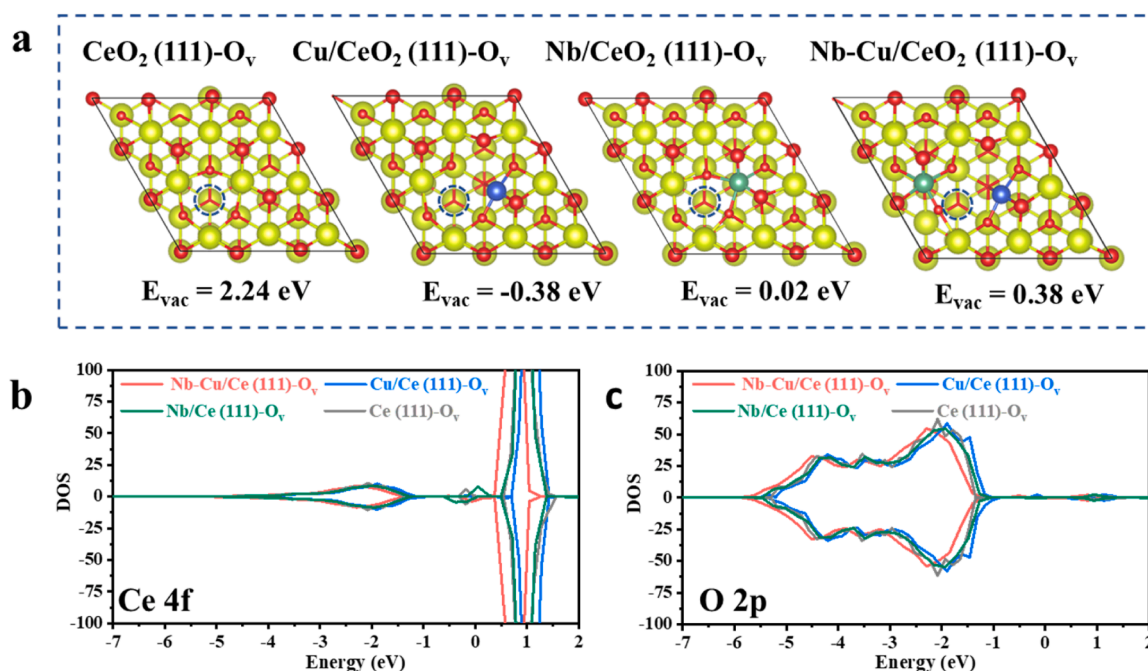


**Fig. 10.** (a) Optimized structures of pure CeO<sub>2</sub> (111), Cu-CeO<sub>2</sub> (111), Nb-CeO<sub>2</sub> (111) and Nb-Cu/CeO<sub>2</sub> (111) with an oxygen vacancy. Red, yellow, blue, and green balls represent O, Ce, Cu, and Nb, respectively.  $E_{vac}$  represents the oxygen vacancy formation energy. The density of states for Ce 4f (b) and O 2p-orbitals (c) of these four model catalysts.

between Ce<sup>3+</sup>, Nb<sup>5+</sup> and Cu<sup>2+</sup> with the assistance of surface oxygen. Furthermore, theoretical modeling coupled with EXAFS analysis and multiple in situ spectroscopic insights reveal that the introduction of proper copper ions in the CeO<sub>2</sub> matrix induces the structure distortion of surface CeO<sub>2</sub>, which is conducive to more niobium ions insertion into the CeO<sub>2</sub>. The embedded Nb synergizes Cu and Ce to evoke the generation of newly adsorptive sites for NO<sub>x</sub> and NH<sub>3</sub> and accelerate the NH<sub>3</sub>-SCR reaction. This work unveils Cu ion docking-triggered Nb incorporation into the CeO<sub>2</sub> lattice meanwhile opens new possibilities for constructing the synergistic catalytic sites in individual catalyst using defective support to achieve important but challenging heterogeneous reactions.

#### CRediT authorship contribution statement

**Yanheng Hao:** Conceptualization, Data curation, Formal analysis, Methodology, Software, Validation, Writing – original draft, Visualization, Writing – review & editing. **Yan Wang:** Validation, Methodology, Writing – original draft, Writing – review & editing, Funding acquisition. **Qi-Yuan Fan:** Performed the theoretical calculations. **Tiantian Zhang:** Methodology. **Yang Liu:** Formal analysis. **Yue Jiang:** Data curation. **Yonghui Gao:** Review. **Zhihui Mao:** Review. **Xiaojun Gu:** Writing – review & editing, Funding acquisition, Resources. **Shanghong Zeng:** Conceptualization, Data curation, Formal analysis, Funding acquisition, Resources, Supervision.

#### Declaration of Competing Interest

The authors declare that they have no known competing financial interests or personal relationships that could have appeared to influence the work reported in this paper.

#### Data availability

Data will be made available on request.

#### Acknowledgments

This work was financially supported by the National Natural Science Foundation of China (21968020 and 22162019), the Natural Science Foundation of Inner Mongolia (2022MS02011), the Science and Technology Project of China Northern Rare Earth (BFXT-2022-D-0023), Independent Project of National Key Laboratory of Baiyunobo Rare Earth Resource Research and Comprehensive Utilization (Grant No. BFXT-2022-D-0043) and Science and Technology Projects of Inner Mongolia Autonomous Region (2021GG0195).

#### Appendix A. Supporting information

Supplementary data associated with this article can be found in the online version at [doi:10.1016/j.apcatb.2023.123254](https://doi.org/10.1016/j.apcatb.2023.123254).

#### References

- [1] Y. Wang, L. Chen, W. Wang, X. Wang, B. Li, S. Zhang, W. Li, S. Li, Revealing the excellent low-temperature activity of the Fe<sub>1-x</sub>Ce<sub>x</sub>O<sub>0.8</sub> catalyst for NH<sub>3</sub>-SCR: improvement of the lattice oxygen mobility, *ACS Appl. Mater. Interfaces* 15 (2023) 17834–17847.
- [2] J. Cheng, D. Zheng, G. Yu, R. Xu, C. Dai, N. Liu, N. Wang, B. Chen, N<sub>2</sub>O catalytic decomposition and NH<sub>3</sub>-SCR coupling reactions over Fe-SSZ-13 catalyst: mechanisms and interactions unraveling via experiments and DFT calculations, *ACS Catal.* 13 (2022) 934–947.
- [3] K. Song, K. Guo, S. Mao, D. Ma, Y. Lv, C. He, H. Wang, Y. Cheng, J.-W. Shi, Insight into the origin of excellent SO<sub>2</sub> tolerance and de-NO<sub>x</sub> performance of quasi-Mn-BTC in the low-temperature catalytic reduction of nitrogen oxide, *ACS Catal.* 13 (2023) 5020–5032.
- [4] W. Xiong, L. Liu, A. Guo, D. Chen, Y. Shan, M. Fu, J. Wu, D. Ye, P. Chen, Economical and Sustainable Synthesis of Small-Pore Chabazite Catalysts for NO<sub>x</sub> Abatement by Recycling Organic Structure-Directing Agents, *Environ. Sci. Technol.* 57 (2023) 655–665.
- [5] S. Chen, R. Xie, Z. Liu, L. Ma, N. Yan, Efficient NO<sub>x</sub> Reduction against Alkali Poisoning over a Self-Protection Armor by Fabricating Surface Ce<sub>2</sub>(SO<sub>4</sub>)<sub>3</sub> Species: Comparison to Commercial Vanadia Catalysts, *Environ. Sci. Technol.* 57 (2023) 2949–2957.
- [6] Y. Long, Y. Su, M. Chen, S. Lu, X. Luo, Z. Zhu, Z. Wu, X. Weng, Polymerization State of Vanadyl Species Affects the Catalytic Activity and Arsenic Resistance of the V<sub>2</sub>O<sub>5</sub>-WO<sub>3</sub>/TiO<sub>2</sub> Catalyst in Multipollutant Control of NO<sub>x</sub> and Chlorinated Aromatics, *Environ. Sci. Technol.* 57 (2023) 7590–7598.

- [7] M. Zhu, J.K. Lai, U. Tumuluri, Z. Wu, I.E. Wachs, Nature of Active Sites and Surface Intermediates during SCR of NO with NH<sub>3</sub> by Supported V<sub>2</sub>O<sub>5</sub>-WO<sub>3</sub>/TiO<sub>2</sub> Catalysts, *J. Am. Chem. Soc.* 139 (2017) 15624–15627.
- [8] Y. Wu, Y. Ma, Y. Wang, K.G. Rappé, N.M. Washton, Y. Wang, E.D. Walter, F. Gao, Rate Controlling in Low-Temperature Standard NH<sub>3</sub>-SCR: Implications from Operando EPR Spectroscopy and Reaction Kinetics, *J. Am. Chem. Soc.* 144 (2022) 9734–9746.
- [9] J. Abdul Nasir, J. Guan, T.W. Keal, A.W. Desmoutier, Y. Lu, A.M. Beale, C.R. A. Catlow, A.A. Sokol, Influence of Solvent on Selective Catalytic Reduction of Nitrogen Oxides with Ammonia over Cu-CHA Zeolite, *J. Am. Chem. Soc.* 145 (2023) 247–259.
- [10] Y. Shan, J. Du, Y. Yu, W. Shan, X. Shi, H. He, Precise control of post-treatment significantly increases hydrothermal stability of in-situ synthesized Cu-zeolites for NH<sub>3</sub>-SCR reaction, *Appl. Catal. B Environ.* 266 (2020), 118655.
- [11] M. Li, M. Gao, G. He, Y. Yu, H. He, Mechanistic Insight into the Promotion of the Low-Temperature NH<sub>3</sub>-Selective Catalytic Reduction Activity over Mn<sub>x</sub>Ce<sub>1-x</sub>O<sub>y</sub> Catalysts: A Combined Experimental and Density Functional Theory Study, *Environ. Sci. Technol.* 57 (2023) 3875–3882.
- [12] L. Schumacher, J. Weyel, C. Hess, Unraveling the Active Vanadium Sites and Adsorbate Dynamics in VO<sub>x</sub>/CeO<sub>2</sub> Oxidation Catalysts Using Transient IR Spectroscopy, *J. Am. Chem. Soc.* 144 (2022) 14874–14887.
- [13] K. Liu, H. He, B. Chu, Microkinetic study of NO oxidation, standard and fast NH<sub>3</sub>-SCR on CeWO at low temperatures, *Chem. Eng. J.* 423 (2021), 130128.
- [14] P. Li, Y. Xin, Q. Li, Z. Wang, Z. Zhang, L. Zheng, Ce-Ti amorphous oxides for selective catalytic reduction of NO with NH<sub>3</sub>: confirmation of Ce-O-Ti active sites, *Environ. Sci. Technol.* 46 (2012) 9600–9605.
- [15] S. Li, Y. Che, L. Liu, Y. Du, X. Wu, Insight into the low-temperature DeNO<sub>x</sub> performance of copper-based oxides: Perspective from the valence state distribution, *J. Catal.* 423 (2023) 154–169.
- [16] B. Liu, J. Liu, L. Xin, T. Zhang, Y. Xu, F. Jiang, X. Liu, Unraveling Reactivity Descriptors and Structure Sensitivity in Low-Temperature NH<sub>3</sub>-SCR Reaction over CeTiO<sub>x</sub> Catalysts: A Combined Computational and Experimental Study, *ACS Catal.* 11 (2021) 7613–7636.
- [17] J. Zhang, L. Chen, Y. Fan, C. Zhao, W. Dai, L. Yang, L. Zhou, J. Zou, X. Luo, Unraveling the high catalytic activity of single atom Mo-doped TiO<sub>2</sub> toward NH<sub>3</sub>-SCR: Synergetic roles of Mo as acid sites and oxygen vacancies as oxidation sites, *Chem. Eng. J.* 465 (2023), 147259.
- [18] Y. Wang, T. Shi, Q.-Y. Fan, Y. Liu, A. Zhang, Z. Li, Y. Hao, L. Chen, F. Liu, X. Gu, S. Zeng, Discovering Surface Structure and the Mechanism of Graphene Oxide-Triggered CeO<sub>2</sub>-WO<sub>3</sub>/TiO<sub>2</sub> Catalysts for NO Abatement with NH<sub>3</sub>, *ACS Catal.* 12 (2022) 8386–8403.
- [19] S. Xie, W. Tan, Y. Li, L. Ma, S.N. Ehrlich, J. Deng, P. Xu, F. Gao, L. Dong, F. Liu, Copper Single Atom-Triggered Niobia–Ceria Catalyst for Efficient Low-Temperature Reduction of Nitrogen Oxides, *ACS Catal.* 12 (2022) 2441–2453.
- [20] S. Li, L. Song, J. Li, H. He, Promotional Mechanisms of Activity and SO<sub>2</sub> Tolerance of NdVO<sub>x</sub>/TiO<sub>2</sub> Catalysts for Selective Catalytic Reduction of NO<sub>x</sub> with NH<sub>3</sub>, *ACS Catal.* 13 (2023) 2867–2884.
- [21] N. Zhang, L. Li, Y. Guo, J. He, R. Wu, L. Song, G. Zhang, J. Zhao, D. Wang, H. He, A MnO<sub>2</sub>-based catalyst with H<sub>2</sub>O resistance for NH<sub>3</sub>-SCR: Study of catalytic activity and reactants-H<sub>2</sub>O competitive adsorption, *Appl. Catal. B Environ.* 270 (2020), 118860.
- [22] J. Liu, X. Shi, Y. Yu, M. Zhang, D. Liu, H. He, Excellent hydrocarbon tolerance of CeO<sub>2</sub>-WO<sub>3</sub>-SnO<sub>2</sub> oxide catalyst for the NH<sub>3</sub>-SCR of NO, *Appl. Catal. B Environ.* 324 (2023), 122283.
- [23] Z.-b Xiong, C. Wu, Q. Hu, Y.-z Wang, J. Jin, C.-m Lu, D.-x Guo, Promotional effect of microwave hydrothermal treatment on the low-temperature NH<sub>3</sub>-SCR activity over iron-based catalyst, *Chem. Eng. J.* 286 (2016) 459–466.
- [24] S. Ali, L. Chen, Z. Li, T. Zhang, R. Li, Su.H. Bakhtiar, X. Leng, F. Yuan, X. Niu, Y. Zhu, Cu-Nb<sub>1-x</sub> (x = 0.45, 0.35, 0.25, 0.15) bimetal oxides catalysts for the low temperature selective catalytic reduction of NO with NH<sub>3</sub>, *Appl. Catal. B Environ.* 236 (2018) 25–35.
- [25] Z. Zhang, Y. Li, P. Yang, Y. Li, C. Zhao, R. Li, Y. Zhu, Improved NH<sub>3</sub>-SCR deNO<sub>x</sub> activity and tolerance to H<sub>2</sub>O & SO<sub>2</sub> at low temperature over the Nb<sub>m</sub>Cu<sub>0.1-m</sub>Ce<sub>0.9</sub>O<sub>x</sub> catalysts: Role of acidity by niobium doping, *Fuel* 303 (2021), 121239.
- [26] L. Xue, C. Zhang, J. Wu, Q.-Y. Fan, Y. Liu, Y. Wu, J. Li, H. Zhang, F. Liu, S. Zeng, Unveiling the reaction pathway on Cu/CeO<sub>2</sub> catalyst for electrocatalytic CO<sub>2</sub> reduction to CH<sub>4</sub>, *Appl. Catal. B Environ.* 304 (2022), 120951.
- [27] S. Cai, T. Xu, P. Wang, L. Han, S. Impeng, Y. Li, T. Yan, G. Chen, L. Shi, D. Zhang, Self-Protected CeO<sub>2</sub>-SnO<sub>2</sub>@SO<sub>4</sub><sup>2-</sup>/TiO<sub>2</sub> Catalysts with Extraordinary Resistance to Alkali and Heavy Metals for NO<sub>x</sub> Reduction, *Environ. Sci. Technol.* 54 (2020) 12752–12760.
- [28] D.W. Kwon, D.H. Kim, S. Lee, J. Kim, H.P. Ha, A dual catalytic strategy by the nature of the functionalization effect as well as active species on vanadium-based catalyst for enhanced low temperature SCR, *Appl. Catal. B Environ.* 289 (2021), 120032.
- [29] G. Kresse, J. Furthmüller, Efficiency of ab-initio total energy calculations for metals and semiconductors using a plane-wave basis set, *Comput. Mater. Sci.* 6 (1996) 15–50.
- [30] G. Kresse, J. Furthmüller, Efficient iterative schemes for ab initio total-energy calculations using a plane-wave basis set, *Phys. Rev. B* 54 (1996) 11169–11186.
- [31] G. Kresse, D. Joubert, From ultrasoft pseudopotentials to the projector augmented-wave method, *Phys. Rev. B* 59 (1999) 1758–1775.
- [32] P.E. Blöchl, Projector augmented-wave method, *Phys. Rev. B* 50 (1994) 17953–17979.
- [33] J.P. Perdew, K. Burke, M. Ernzerhof, Generalized Gradient Approximation Made Simple, *Phys. Rev. Lett.* 77 (1996) 3865–3868.
- [34] H.-M. Zhang, Q.-Y. Fan, Q.-H. Zhang, J.-C. Kang, Y. Wang, J. Cheng, Understanding Catalytic Mechanisms of Alkane Oxidation from the Perspective of Energy Levels, *J. Phys. Chem. C* 124 (2020) 6070–6077.
- [35] Y.-Q. Su, I.A.W. Filot, J.-X. Liu, I. Tranca, E.J.M. Hensen, Charge Transport over the Defective CeO<sub>2</sub>(111) Surface, *Chem. Mater.* 28 (2016) 5652–5658.
- [36] S. Singh, D. Bhatia, Modeling the role of CO and C<sub>3</sub>H<sub>6</sub> in NO<sub>x</sub> reduction on a Cu-CHA SCR catalyst, *Chem. Eng. J.* 377 (2019), 120311.
- [37] R. You, X. Zhang, L. Luo, Y. Pan, H. Pan, J. Yang, L. Wu, X. Zheng, Y. Jin, W. Huang, NbO<sub>x</sub>/CeO<sub>2</sub>-rods catalysts for oxidative dehydrogenation of propane: Nb–CeO<sub>2</sub> interaction and reaction mechanism, *J. Catal.* 348 (2017) 189–199.
- [38] Y. Jiang, T. Liu, W. Gao, H. Ge, Z. Yang, R. Lin, X. Gu, S. Wang, Three-dimensionally ordered macroporous Ce-W-Nb oxide catalysts for selective catalytic reduction of NO with NH<sub>3</sub>, *Chem. Eng. J.* 433 (2022), 134576.
- [39] B. Qin, R.-t Guo, L.-g Wei, X.-f Yin, T.-y Yin, J. Zhou, Z.-z Qiu, A highly effective NbMnCeO<sub>x</sub> catalyst for NH<sub>3</sub>-SCR and in situ DRIFTS for investigating the reaction mechanism, *J. Environ. Chem. Eng.* 10 (2022), 108564.
- [40] D. An, Y. Yang, W. Zou, Y. Cai, Q. Tong, J. Sun, L. Dong, Insight into the promotional mechanism of Cu modification towards wide-temperature NH<sub>3</sub>-SCR performance of NbCe catalyst, *Chin. Chem. Eng. J.* 50 (2022) 301–309.
- [41] J. Ding, C. Xu, G. Fan, T. Naren, Y. Wang, Y. Liu, X. Gu, L. Wu, S. Zeng, Engineering CeO<sub>2</sub> configurations to regulate the CuO dispersion and switch pathways of preferential CO oxidation, *Appl. Catal. B Environ.* 331 (2023), 122686.
- [42] S. Zeng, Y. Wang, S. Ding, J.J.H.B. Sattler, E. Borodina, L. Zhang, B. M. Weckhuysen, H. Su, Active sites over CuO/CeO<sub>2</sub> and inverse CeO<sub>2</sub>/CuO catalysts for preferential CO oxidation, *J. Power Sour.* 256 (2014) 301–311.
- [43] D. Kang, X. Yu, M. Ge, Morphology-dependent properties and adsorption performance of CeO<sub>2</sub> for fluoride removal, *Chem. Eng. J.* 330 (2017) 36–43.
- [44] A. Martínez-Arias, M. Fernández-García, L.N. Salamanca, R.X. Valenzuela, J. C. Conesa, J. Soria, Structural and Redox Properties of Ceria in Alumina-Supported Ceria Catalyst Supports, *J. Phys. Chem. B* 104 (2000) 4038–4046.
- [45] J. Lu, J. Wang, Q. Zou, D. He, L. Zhang, Z. Xu, S. He, Y. Luo, Unravelling the Nature of the Active Species as well as the Doping Effect over Cu/Ce-Based Catalyst for Carbon Monoxide Preferential Oxidation, *ACS Catal.* 9 (2019) 2177–2195.
- [46] R. Qu, X. Gao, K. Cen, J. Li, Relationship between structure and performance of a novel cerium-niobium binary oxide catalyst for selective catalytic reduction of NO with NH<sub>3</sub>, *Appl. Catal. B Environ.* 142–143 (2013) 290–297.
- [47] W. Zhang, X. Shi, Z. Yan, Y. Shan, Y. Zhu, Y. Yu, H. He, Design of High-Performance Iron–Niobium Composite Oxide Catalysts for NH<sub>3</sub>-SCR: Insights into the Interaction between Fe and Nb, *ACS Catal.* 11 (2021) 9825–9836.
- [48] W. Tan, C. Wang, S. Yu, Y. Li, S. Xie, F. Gao, L. Dong, F. Liu, Revealing the effect of paired redox-acid sites on metal oxide catalysts for efficient NO removal by NH<sub>3</sub>-SCR, *J. Hazard. Mater.* 416 (2021), 125826.
- [49] L.E. Gevers, L.R. Enakonda, A. Shahid, S. Ould-Chikh, C.I.Q. Silva, P.P. Paalanen, A. Aguilar-Tapia, J.L. Hazemann, M.N. Hedhili, F. Wen, J. Ruiz-Martinez, Unraveling the structure and role of Mn and Ce for NO<sub>x</sub> reduction in application-relevant catalysts, *Nat. Commun.* 13 (2022) 2960.
- [50] J. Fan, X. Wu, X. Wu, Q. Liang, R. Ran, D. Weng, Thermal ageing of Pt on low-surface-area CeO<sub>2</sub>-ZrO<sub>2</sub>-La<sub>2</sub>O<sub>3</sub> mixed oxides: Effect on the OSC performance, *Appl. Catal. B Environ.* 81 (2008) 38–48.
- [51] J. Li, Y. Han, Y. Zhu, R. Zhou, Purification of hydrogen from carbon monoxide for fuel cell application over modified mesoporous CuO–CeO<sub>2</sub> catalysts, *Appl. Catal. B Environ.* 108 109 (2011) 72–80.
- [52] Z. Wang, Z. Qu, X. Quan, Z. Li, H. Wang, R. Fan, Selective catalytic oxidation of ammonia to nitrogen over CuO–CeO<sub>2</sub> mixed oxides prepared by surfactant-templated method, *Appl. Catal. B Environ.* 134 135 (2013) 153–166.
- [53] B. Qin, R.-t Guo, J. Zhou, L.-g Wei, T.-y Yin, W.-g Pan, Promotional role of Nb modification on CuCeO<sub>x</sub> catalyst for low temperature selective catalytic reduction of NO with NH<sub>3</sub>: A mechanism investigation, *Fuel* 329 (2022), 125390.
- [54] P. Wang, S. Chen, S. Gao, J. Zhang, H. Wang, Z. Wu, Niobium oxide confined by ceria nanotubes as a novel SCR catalyst with excellent resistance to potassium, phosphorus, and lead, *Appl. Catal. B Environ.* 231 (2018) 299–309.
- [55] K.A. Resende, A.H. Braga, F.B. Noronha, C.E. Hori, Hydrodeoxygenation of phenol over Ni/Ce<sub>1-x</sub>Nb<sub>x</sub>O<sub>2</sub> catalysts, *Appl. Catal. B Environ.* 245 (2019) 100–113.
- [56] Z. Ma, X. Wu, Z. Si, D. Weng, J. Ma, T. Xu, Impacts of niobia loading on active sites and surface acidity in NbO/CeO<sub>2</sub>-ZrO<sub>2</sub> NH<sub>3</sub>-SCR catalysts, *Appl. Catal. B Environ.* 179 (2015) 380–394.
- [57] M. Kang, E.D. Park, J.M. Kim, J.E. Yie, Manganese oxide catalysts for NO<sub>x</sub> reduction with NH<sub>3</sub> at low temperatures, *Appl. Catal. A Gen.* 327 (2007) 261–269.
- [58] S. Ma, W. Gao, Z. Yang, R. Lin, X. Wang, X. Zhu, Y. Jiang, Superior Ce–Nb–Ti oxide catalysts for selective catalytic reduction of NO with NH<sub>3</sub>, *J. Energy Inst.* 94 (2021) 73–84.
- [59] D. An, Y. Yang, W. Zou, Y. Cai, Q. Tong, J. Sun, L. Dong, Insight into the promotional mechanism of Cu modification towards wide-temperature NH<sub>3</sub>-SCR performance of NbCe catalyst, *Chin. Chem. Eng. J.* 50 (2022) 301–309.
- [60] P. Lu, R. Li, Y. Xing, Y. Li, T. Zhu, H. Yue, W. Wu, Low temperature selective catalytic reduction of NO<sub>x</sub> with NH<sub>3</sub> by activated coke loaded with Fe<sub>2</sub>Co<sub>2</sub>Ce<sub>2</sub>O<sub>m</sub>: The enhanced activity, mechanism and kinetics, *Fuel* 233 (2018) 188–199.
- [61] N.Y. Topsoe, Mechanism of the selective catalytic reduction of nitric oxide by ammonia elucidated by in situ on-line fourier transform infrared spectroscopy, *Science* 265 (1994) 1217–1219.
- [62] G. Landi, P.S. Barbato, A. Di Benedetto, L. Lisi, Optimization of the preparation method of CuO/CeO<sub>2</sub> structured catalytic monolith for CO preferential oxidation in H<sub>2</sub>-rich streams, *Appl. Catal. B Environ.* 181 (2016) 727–737.

- [63] S. Pengpanich, V. Meeyoo, T. Rirksomboon, J. Schwank, The effect of Nb loading on catalytic properties of Ni/Ce<sub>0.75</sub>Zr<sub>0.25</sub>O<sub>2</sub> catalyst for methane partial oxidation, *J. Nat. Gas. Chem.* 16 (2007) 227–234.
- [64] C. Muhich, A. Steinfeld, Principles of doping ceria for the solar thermochemical redox splitting of H<sub>2</sub>O and CO<sub>2</sub>, *J. Mater. Chem. A* 5 (2017) 15578–15590.
- [65] J. Liu, G.-q Li, Y.-f Zhang, X.-q Liu, Y. Wang, Y. Li, Novel Ce-W-Sb mixed oxide catalyst for selective catalytic reduction of NO<sub>x</sub> with NH<sub>3</sub>, *Appl. Surf. Sci.* 401 (2017) 7–16.
- [66] L. Li, L. Zhang, K. Ma, W. Zou, Y. Cao, Y. Xiong, C. Tang, L. Dong, Ultra-low loading of copper modified TiO<sub>2</sub>/CeO<sub>2</sub> catalysts for low-temperature selective catalytic reduction of NO by NH<sub>3</sub>, *Appl. Catal. B Environ.* 207 (2017) 366–375.
- [67] L. Zhang, L. Li, Y. Cao, X. Yao, C. Ge, F. Gao, Y. Deng, C. Tang, L. Dong, Getting insight into the influence of SO<sub>2</sub> on TiO<sub>2</sub>/CeO<sub>2</sub> for the selective catalytic reduction of NO by NH<sub>3</sub>, *Appl. Catal. B Environ.* 165 (2015) 589–598.
- [68] J. Ji, N. Gao, W. Song, Y. Tang, Y. Cai, L. Han, L. Cheng, J. Sun, S. Ma, Y. Chu, C. Tang, L. Dong, Understanding the temperature-dependent H<sub>2</sub>O promotion effect on SO<sub>2</sub> resistance of MnO-CeO<sub>2</sub> catalyst for SCR denitration, *Appl. Catal. B Environ.* 324 (2023) 1222.
- [69] J. Cao, C. Nannuzzi, W. Liu, H. Wu, Y. Gao, R. Zhong, Q. Liu, G. Berlier, Improving the tolerance to alkali and alkaline earth metal chlorides of WO<sub>3</sub> and Nb<sub>2</sub>O<sub>5</sub> promoted V<sub>2</sub>O<sub>5</sub>/TiO<sub>2</sub> catalysts for the NH<sub>3</sub>-SCR reaction, *Fuel* 328 (2022), 125262.
- [70] L.J. Burcham, J. Datka, I.E. Wachs, In situ vibrational spectroscopy studies of supported niobium oxide catalysts, *J. Phys. Chem. B* 103 (1999) 6015–6024.
- [71] J. Liu, X. Li, Q. Zhao, J. Ke, H. Xiao, X. Lv, S. Liu, M. Tadé, S. Wang, Mechanistic investigation of the enhanced NH<sub>3</sub>-SCR on cobalt-decorated Ce-Ti mixed oxide: In situ FTIR analysis for structure-activity correlation, *Appl. Catal. B Environ.* 200 (2017) 297–308.
- [72] S. Ding, F. Liu, X. Shi, H. He, Promotional effect of Nb additive on the activity and hydrothermal stability for the selective catalytic reduction of NO with NH<sub>3</sub> over CeZrO catalyst, *Appl. Catal. B Environ.* 180 (2016) 766–774.
- [73] L. Chen, J. Li, M. Ge, DRIFT study on cerium-tungsten/titania catalyst for selective catalytic reduction of NO<sub>x</sub> with NH<sub>3</sub>, *Environ. Sci. Technol.* 44 (2010) 9590–9596.
- [74] A. Trovarelli, Catalytic Properties of Ceria and CeO<sub>2</sub>-Containing Materials, *Catal. Rev.* 38 (1996) 439–520.
- [75] Z. Liu, J. Zhu, J. Li, L. Ma, S.I. Woo, Novel Mn-Ce-Ti mixed-oxide catalyst for the selective catalytic reduction of NO<sub>x</sub> with NH<sub>3</sub>, *ACS Appl. Mater. Interfaces* 6 (2014) 14500–14508.
- [76] Y. Li, Z. Zhang, X. Zhao, Z. Liu, T. Zhang, X. Niu, Y. Zhu, Effects of Nb-modified CeVO<sub>4</sub> to form surface Ce-O-Nb bonds on improving low-temperature NH<sub>3</sub>-SCR deNO activity and resistance to SO<sub>2</sub> & H<sub>2</sub>O, *Fuel* 331 (2023), 125799.
- [77] Q. Wang, J. Gong, H. Zhang, Q.-Y. Fan, L. Xue, J. Wu, J. Li, Y. Wang, Z. Liu, R. Gao, S. Zeng, Co-promotion of two-type active sites: PtCu single-atom alloy and copper-ceria interface for preferential oxidation of CO, *Appl. Catal. B Environ.* 306 (2022), 121117.
- [78] F. Wang, P. Wang, T. Lan, Y. Shen, W. Ren, D. Zhang, Ultralow-Temperature NO<sub>x</sub> Reduction over SmMn<sub>2</sub>O<sub>5</sub> Mullite Catalysts Via Modulating the Superficial Dual-Functional Active Sites, *ACS Catal.* 12 (2022) 7622–7632.
- [79] J. Shen, S. Lauterbach, C. Hess, Rational Design of Mesoporous CuO-CeO<sub>2</sub> Catalysts for NH<sub>3</sub>-SCR Applications Guided by Multiple In Situ Spectroscopies, *ACS Appl. Mater. Interfaces* 14 (2022) 43407–43420.
- [80] M.R. McCoustra, Water at interfaces, *Phys. Chem. Chem. Phys.* 10 (2008) 4676–4677.
- [81] W.W. Rudolph, C.C. Pye, Gallium(III) hydration in aqueous solution of perchlorate, nitrate and sulfate. Raman and 71-Ga NMR spectroscopic studies and ab initio molecular orbital calculations of gallium(III) water clusters, *Phys. Chem. Chem. Phys.* 4 (2002) 4319–4327.
- [82] A.M. Shahin, F. Grandjean, G.J. Long, T.P. Schuman, Cerium LIII-Edge XAS Investigation of the Structure of Crystalline and Amorphous Cerium Oxides, *Chem. Mater.* 17 (2004) 315–321.
- [83] N. Chubar, V. Gerda, D. Banerjee, G. Yablokova, Effect of Fe(II)/Ce(III) dosage ratio on the structure and anion adsorptive removal of hydrothermally precipitated composites: Insights from EXAFS/XANES, XRD and FTIR, *J. Colloid Interface Sci.* 487 (2017) 388–400.
- [84] A. Froideval, C. Degueldre, C.U. Segre, M.A. Pouchon, D. Grolimund, Niobium speciation at the metal/oxide interface of corroded niobium-doped Zircalloys: A X-ray absorption near-edge structure study, *Corros. Sci.* 50 (2008) 1313–1320.
- [85] S. Ghoshal, Q. Jia, M.K. Bates, J. Li, C. Xu, K. Gath, J. Yang, J. Waldecker, H. Che, W. Liang, G. Meng, Z.-F. Ma, S. Mukerjee, Tuning Nb–Pt Interactions To Facilitate Fuel Cell Electrocatalysis, *ACS Catal.* 7 (2017) 4936–4946.
- [86] N.M. Phadke, J. Van der Mynsbrugge, E. Mansoor, A.B. Getsoian, M. Head-Gordon, A.T. Bell, Characterization of Isolated Ga<sup>3+</sup> Cations in Ga/H-MFI Prepared by Vapor-Phase Exchange of H-MFI Zeolite with GaCl<sub>3</sub>, *ACS Catal.* 8 (2018) 6106–6126.
- [87] L. Szabova, M.F. Camellone, M. Huang, V. Matolin, S. Fabris, Thermodynamic, electronic and structural properties of Cu/CeO<sub>2</sub> surfaces and interfaces from first-principles DFT+U calculations, *J. Chem. Phys.* 133 (2010), 234705.